

The radioscience LaRa instrument onboard ExoMars 2020 to investigate the rotation and interior of Mars

V. Dehant^{1,2}, S. Le Maistre¹, R.-M. Baland¹, N. Bergeot¹, O. Karatekin¹, M.-J. Péters¹, A. Rivoldini¹, L. Ruiz Lozano^{2,1}, O. Temel¹, T. Van Hoolst¹, M. Yseboodt¹, M. Mitrovic¹, A.S. Kosov³, V. Valenta⁴, L. Thomassen⁵, S. Karki², K. Al Khalifeh², C. Craeye², L.I. Gurvits^{6,7}, J.-C. Marty⁸, S. Asmar⁹, W. Folkner⁹,
and the LaRa team (<http://lara.oma.be/team>)¹

¹Royal Observatory of Belgium, Brussels, 3 avenue Circulaire, B1180 Brussels, Belgium, v.dehant@oma.be

²Université catholique de Louvain, Belgium

³IKI - Space Research Institute of Russian Academy of Sciences, Moscow, Russia

⁴European Space Research and Technology Centre (ESTEC), ESA, The Netherlands

⁵AntwerpSpace, OHB Company, Belgium

⁶JIVE - Joint Institute for VLBI ERIC (European Research Infrastructure Consortium), The Netherlands

⁷Department of Astrodynamics and Space Missions, Delft University of Technology, The Netherlands

⁸Observatoire Midi-Pyrénées, GRGS, CNES, France

⁹Jet Propulsion Laboratory, California Institute of Technology, Pasadena, USA

Accepted in PSS, October 2019

Abstract

LaRa (Lander Radioscience) is an experiment on the ExoMars 2020 mission that uses the Doppler shift on the radio link due to the motion of the ExoMars platform tied to the surface of Mars with respect to the Earth ground stations (e.g. the deep space network stations of NASA), in order to precisely measure the relative velocity of the lander on Mars with respect to the Earth. The LaRa measurements shall improve the understanding of the structure and processes in the deep interior of Mars by obtaining the rotation and orientation of Mars with a better precision compared to the previous missions. In this paper, we provide the analysis done until now for the best realization of these objectives. We explain the geophysical observation that will be reached with LaRa (Length-of-day variations, precession, nutation, and possibly polar motion). We develop the experiment set up, which includes the ground stations on Earth (so-called ground segment). We describe the instrument, i.e. the transponder and its three antennas. We further detail the link budget and the expected noise level that will be reached. Finally, we detail the expected results, which encompasses the explanation of how we shall determine Mars' orientation parameters, and the way we shall deduce Mars' interior structure and Mars' atmosphere from them. Lastly, we explain briefly how we will be able to determine the Surface platform position.

1 Introduction

Shortly after their formation, Earth and Mars might have been very similar. Nowadays, those neighboring planets show some differences proving that they have evolved differently.

For example, Mars has a tenuous atmosphere mainly made of CO_2 and containing in average almost no oxygen. An important part of its surface has been generated a long time ago (before 4 Ga) and shows no sign of regional-scale recent alteration, while the Earth’s surface is continuously recycled through plate tectonics. Mars is monoplate. Mars is presently and since the Noachian (≈ 3.5 Ga), a very dry planet. All this indicates that both planets, while being quite similar terrestrial planets, also differ internally. For instance, although it is known from observation of the tidal k_2 Love number from orbiters (for the first time determined by Yoder et al. (2003)) that Mars’ iron-rich core has a radius of about 1794 ± 65 km at one sigma (range [1600 km, 1990 km] for 3 sigma, (Smrekar et al., 2019)), its composition and the planet’s thermal state are not well known. The present uncertainty on the core radius and the not-well-known lower mantle temperature have major consequences for the understanding of the global interior structure and dynamics and of the planetary evolution. For example, for a bridgmanite lower mantle to exist in Mars, the liquid core must be sufficiently small. If present, the endothermic ringwoodite-bridgmanite phase transition would have a focusing effect on mantle convection, which could help formation and maintaining Tharsis (Harder and Christensen, 1996; van Thienen et al., 2005, 2006). The thermal state and composition of the core are also important for the history of the magnetic dynamo, which in turn could have important consequences for the retention of the atmosphere and the possible habitability of the surface early in Mars’ history.

We are interested in investigating how and why Mars differs from Earth. To that aim, we have designed an experiment addressing the deep interior, essentially the core, and the atmosphere dynamics: the LaRa (Lander Radioscience) experiment. LaRa is the generic name for the transponder and its antennas (see Fig. 1) that will be included in the payload elements on the Surface Platform (SP, also called Kazachok Platform) of the ExoMars 2020 mission led by ESA and Roscosmos. The experiment uses a coherent X-band transponder on Mars to obtain two-way Doppler measurements, i.e. to measure the line-of-sight velocity variations between the SP and the Earth station, and is designed to obtain measurements over at least one Martian year (687 Earth days). These Doppler measurements, in conjunction with other previous or simultaneous direct-to-Earth (DTE) radio link measurements, will be used to obtain Mars’ rotational behavior (precession, nutations, length-of-day (LOD) variations, and polar motion). More specifically, measuring the relative position of the SP on the surface of Mars with respect to the terrestrial ground stations allows reconstructing Mars’ time-varying orientation and rotation in inertial space, knowing the Earth’s orientation precisely (i.e., Earth’s precession, nutation, polar motion, and length-of-day variations). These precise measurements are used to determine the inertia of the whole planet (mantle plus core), the moment of inertia (MoI) of the core, and the global-scale seasonal changes of the atmosphere (variation of the angular momentum and inertia due to the seasonal mass transfer of CO_2 between the atmosphere and ice caps, thus informing about the atmosphere dynamics).

The LaRa experiment will be conducted jointly with the other experiments of the ExoMars missions as well as of the NASA InSight mission (Interior Exploration using Seismic Investigations, Geodesy and Heat Transport) in order to obtain the maximum amount of information about the interior of Mars and consequently on its formation and evolution, in accordance with the ExoMars objective to investigate the planet’s deep interior to better understand Mars’ evolution and habitability, as well as to investigate the Martian atmosphere.

The paper is organized as follows: Section 2 provides the scientific rationale, including Mars’ rotation model, interior structure, and atmosphere dynamics. Section 3 describes

the history of the LaRa experiment, its objectives, the LaRa team, the transponder and the antennas, the ground segment, the link budget, the measurements, and the operations. The experiment involves an important ground segment, which includes the Deep Space Network (DSN) and the ESA TRACKing stations (ESTRACK). Complementary observation will be performed by VLBI (Very Long Baseline Interferometry) radiotelescopes in the frame of the Planetary Radio Interferometry and Doppler Experiment (PRIDE) (see Section 3.8). Section 4 summarizes the expected results of the LaRa experiment: the improvement expected for the MOP (Mars Orientation and rotation Parameters) determination and the consequences for our understanding of Mars' interior structure and atmosphere dynamics. The capability of LaRa to accurately locate the lander at the surface of Mars after few days at the surface is also addressed in this section.

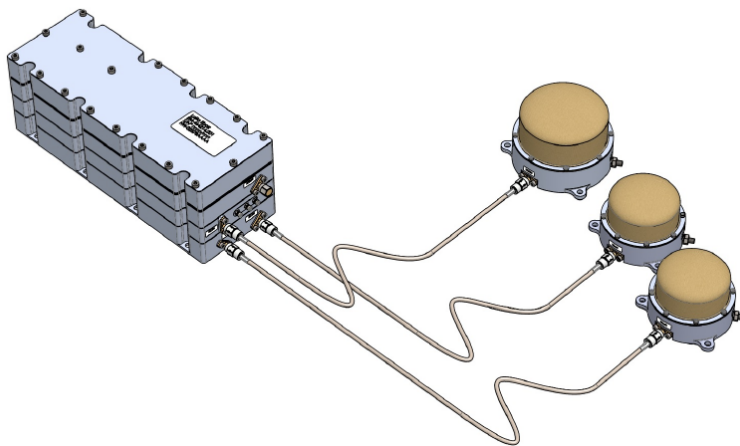


Figure 1: LaRa assembly consisting of a transponder and 3 antennas that are interconnected via 3 coaxial cables.

2 Mars rotation

The variations in the rotation of Mars can be separated into (1) the variations in the rotation about the spin axis, (2) the variations of spin axis with respect to inertial space (variations in orientation of the spin axis in space), and (3) the changes of the spin axis relative to body-fixed axes. LaRa will improve current estimates of those variations or measure them for the first time, to yield information on the interior structure and atmosphere of Mars, as described in the introduction.

2.1 Rotation model of Mars

The rotation of Mars is described by the temporal evolution of the Euler angles from an Inertial Frame (IF) to the rotating Body Frame (BF) of Mars (i.e., a frame tied to the planet), or from the IF to a reference frame attached to the angular momentum (AM) axis, which is very close to the spin axis (Bouquillon and Souchay, 1999). Those angles are the node longitude ψ , the obliquity ε , and the rotation angle ϕ (see Fig. 2). The IF is here chosen to be associated with the mean orbital plane of Mars at a reference epoch (J2000.0). The BF is attached to the principal axes of inertia of the planet, and therefore associated with the equator of figure of Mars. In models of the rotation of Mars, the planet is often first considered to respond rigidly to rotational forcing. Small non-rigid contributions are added afterwards. For a non-rigid Mars, the BF is attached to the mean principal axes of the mantle. In the next three subsections, the different rotation characteristics of Mars

Table 1: List of acronyms used in the paper.

ADEV	Allan deviation
AM	Angular Momentum
ATDF	Ascii Test Data Format
BELSPPO	Belgian Federal Science Policy Office
BF	Body Frame
BIP	Acronym for the Onboard Information and Memory unit in Russian
CDR	Critical Design Review
CW	Chandler wobble
DSN	Deep Space Network
DTE	Direct-to-Earth
DW	Mantle mineralogy composition from Taylor et al. (2013) starting from the model of Dreibus & Wänke (1984, 1987) and Wänke & Dreibus (1988, 1994), and adding further laboratory data, see (Taylor, 2013) and references in that paper
ESOC	European Space Operations Centre
ESTRACK	ESA's European Space TRACKing network
EH45	Mantle mineralogy composition from Sanloup et al. (1999) using intermediate chondrites between H ordinary chondrites and EH enstatite chondrites (Sanloup et al., 1999) (EH45:E55)
EVN	European VLBI Network
FCN	Free Core Nutation
FICN	Free Inner Core Nutation
GEP	Geophysics and Environmental Package
GINS	Géodésie par Intégrations Numériques Simultanées
ICRF	International Celestial Reference Frame
IF	Inertial Frame
IKI RAS	Space Research Institute of the Russian Academy of Sciences
InSight	Interior Exploration using Seismic Investigations, Geodesy and Heat Transport
ITU	International Telecommunication Union
JIVE	Joint Institute for VLBI European Research Infrastructure Consortium
JUICE	JUpter ICy moons Explorer
LaRa	Lander Radioscience
LF	Mantle mineralogy composition from Lodders and Fegley (1997) (Lodders and Fegley, 1997)
LO	Local oscillator
LOD	Length of Day
MA	Mantle mineralogy composition from Morgan and Anders (1979) (Morgan and Anders, 1979)
MM	Mantle mineralogy composition from Mohapatra and Murty (2003) (Mohapatra and Murty, 2003)
MoI	Moment of inertia
MOP	Mars Orientation and rotation Parameters
NEIGE	NEtlander Ionosphere and Geodesy Experiment
ODF	Operation Data File - Orbit Data File
PM	Polar Motion
PRIDE	Planetary Radio Interferometry and Doppler Experiment
PRODEX	PROgramme for the Development of scientific EXperiments
RGS	Russian ground station
RHU	Radioisotope Heater Unit
RISE	Rotation and Interior Structure Experiment
ROB	Royal Observatory of Belgium
SEIS	The ExoMars seismometer
SNR	Signal-to-noise ratio
SP	Surface Platform
SSPA	Solid-State Power Amplifier
TDM	Technical Data Measurement file - Tracking Data Message
TNF	Tracking and Navigation data File
TU Delft	Delft University of Technology
TVAC	Thermal and Vacuum test
VLBI	Very Long Baseline Interferometry

will be defined. The relation with the interior structure and atmosphere is described in sections 2.2 and 2.3.

2.1.1 Length-of-day variations

The temporal variations of the rotation angle ϕ can be decomposed into a uniform rotation and periodic variations:

$$\phi = \phi_0 + \Omega_0 t + \Delta\phi \quad (1)$$

where t is the time past the J2000 epoch, ϕ_0 is such that the X -axis points in the direction of the prime meridian at J2000.0, and $\Omega_0 = 350^\circ.89/\text{day}$ is the constant rate of uniform rotation (Archinal et al., 2018). $\Delta\phi$ are the variations induced mainly by the exchanges of angular momentum between the atmosphere and the planet due to the seasonal CO_2 sublimation and condensation processes at polar caps, mass re-distributions in the atmosphere, and seasonally changing winds. $\Delta\phi$ can be written as a series

$$\Delta\phi = \sum_m \phi_m^c \cos(f_m t) + \phi_m^s \sin(f_m t), \quad (2)$$

with f_m , the main frequencies associated to seasonal processes (*e.g.* annual, semi-annual), and $\phi_m^{c/s}$, the amplitudes associated with each frequency f_m (see Section 2.3).

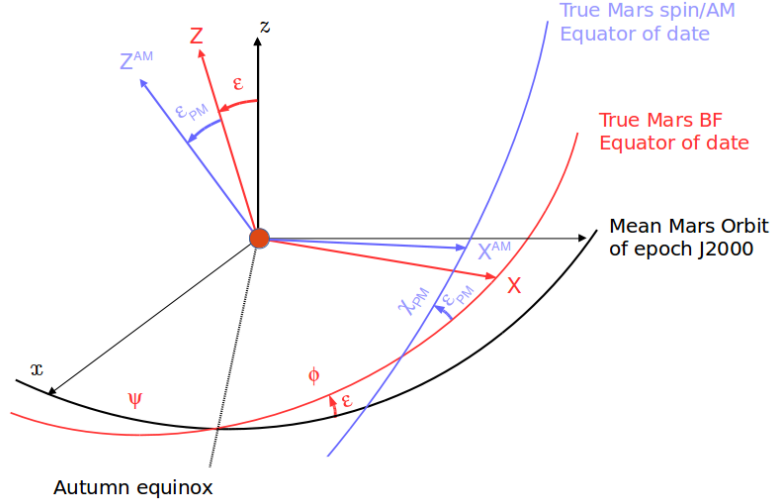


Figure 2: Euler angles (defined as prograde angles) between the Martian rotating BF (axes XYZ) and the IF associated to the Martian mean orbit at epoch J2000.0 (axes xyz). The X -axis of the BF is chosen as the prime meridian defined in the IAU (International Astronomical Union) convention (Archinal et al., 2018). ψ is measured from the x -axis to the autumn equinox, ϕ is measured from the equinox to the X -axis, and ε is the angle from the z -axis to the Z -axis, or the inclination of the BF equator over the IF equator. The spin axis does not coincide with the figure axis of Mars. They are inclined by ε_{PM} to each other, and χ_{PM} is measured from the node of the spin equator over the BF equator to the X^{AM} -axis (the subscript PM stands for *Polar Motion*). The angular momentum axis can be considered as aligned to the spin axis (Bouquillon and Souchay, 1999).

Since deviations from the orientation given by the uniform rotation imply changes in the length of a day, it is customary to use length-of-day (LOD) variations $\Delta LOD = 2\pi/(\frac{d\phi}{dt}) - \frac{2\pi}{\Omega_0}$. The mean LOD variation, averaged over many years has been measured by combining Viking and Pathfinder data with the tracking of Mars orbiters: Mars Global Surveyor (MGS), Mars Odyssey (ODY) and Mars Reconnaissance Orbiter (MRO) (Konopliv et al., 2006, 2011b, 2016). LaRa will improve current estimates of the LOD variations (known to within about 15%, Konopliv et al. (2011b)), give insight on interannual variations and provide global constraints on the distribution of atmospheric mass, angular momentum, and the ice caps.

2.1.2 Precession and nutations

Since Mars is tilted in space (the Z -axis of the BF is not parallel to the z -axis of the IF ($\varepsilon \simeq 25^\circ$)), flattened and rotating, it reacts as a spinning top to the gravitational torque exerted by the Sun. Because of the orbital eccentricity of Mars and of the orbital changes due to interactions with other planets, the Solar gravitational torque on Mars changes periodically with time. The other planets, as well as Phobos and Deimos, the two natural satellites of Mars, also exert direct gravitational torques on Mars.

As a consequence, the angles ψ and ε , change with time at various time-scales. The angle ψ can be decomposed into a slow uniform precession around the z -axis (see Fig. 3) at rate $\dot{\psi}$ and periodic nutations in longitude $\Delta\psi$. Referring the nutations with respect to the J2000 mean equinox, the longitude is defined as $\psi = \dot{\psi}t + \Delta\psi$. The angle ε is the sum of the J2000.0 value ε_0 and of periodic nutations in obliquity $\Delta\varepsilon$. The time needed to perform one precession cycle around the orbit normal is about 171,000 years ($\dot{\psi} \simeq -7.6$ arcsecond/year). A first objective of LaRa is to very accurately determine the

precession rate. Since $\dot{\psi}$ is inversely proportional to the polar principal moment of inertia (MoI), LaRa will be able to provide accurate constraints on the interior structure. This has already been performed by using the Viking Lander radio link (Yoder and Standish (1997)) together with Pathfinder spacecraft radio-link (Folkner et al. (1997b)), combined with orbiter data (Konopliv et al. (2006, 2011b, 2016)), as well as by using the MERs (Mars Exploration Rovers) when fixed (Kuchynka et al. (2014); Le Maistre (2013)). The present uncertainty on the precession rate (Konopliv et al. (2016)) of 2.1 mas/year, corresponding to a period change of about 47 years, will be improved by an order of magnitude (up to 0.3 mas/year) by using LaRa and RISE (Rotation and Interior Structure Experiment, onboard the InSight NASA mission landed on Mars in 2018) data, see Table 4.

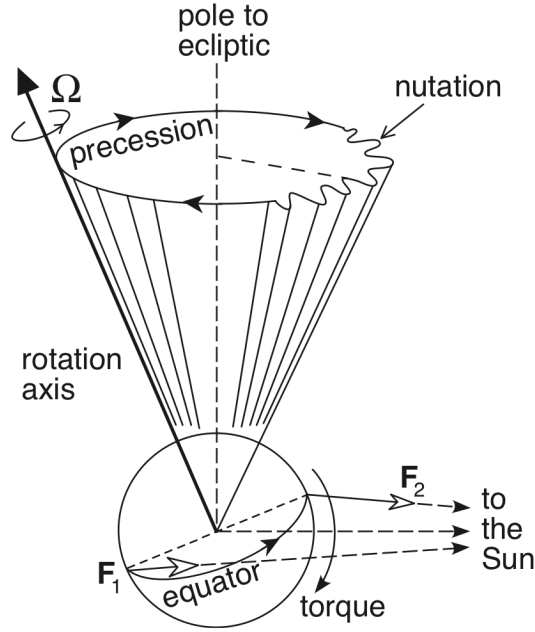


Figure 3: Precession and nutations of the rotation axis about the orbit pole (Lowrie, 2011)

The resulting motion due to precession and nutation is wiggly as illustrated in Fig. 3. In practice, the variables ψ and ε are often related to $(\delta x, \delta y)$, the projection of the trajectory of a unit vector along the figure axis onto the J2000 mean BF equator (Defraigne et al., 1995). The mean BF is defined so that it follows the uniform precession but not the nutations. At first order in small variations, around J2000, that projection can be written as

$$(\delta x, \delta y) = (\sin \varepsilon_o (\dot{\psi} t + \Delta\psi), -\Delta\varepsilon). \quad (3)$$

where the precession rate $\dot{\psi}$ is usually omitted to focus on the nutations. It can be expressed as series of prograde and retrograde circular motions

$$\begin{Bmatrix} \delta x \\ \delta y \end{Bmatrix} = \sum_j \left(\mathcal{P}_j \begin{Bmatrix} \cos \\ \sin \end{Bmatrix} (f_j t + \pi_j^0) + \mathcal{R}_j \begin{Bmatrix} \cos \\ \sin \end{Bmatrix} (-f_j t - \rho_j^0) \right) \quad (4)$$

whose amplitudes \mathcal{P}_j and \mathcal{R}_j and phases π_j^0 and ρ_j^0 at J2000 are related to the amplitudes and phases of similar series for the longitude and obliquity nutations such as those computed by (Reasenberg and King, 1979) for Mars figure axis, or those of Bouquillon and Souchay (1999) or Roosbeek (1999) for Mars AM axis, and expressed as

$$\begin{Bmatrix} \Delta\psi \\ \Delta\varepsilon \end{Bmatrix} = \sum_j \left(\begin{Bmatrix} \psi_j^c \\ \varepsilon_j^c \end{Bmatrix} \cos \varphi_j + \begin{Bmatrix} \psi_j^s \\ \varepsilon_j^s \end{Bmatrix} \sin \varphi_j \right) \quad (5)$$

The arguments $\varphi_j = f_j t + \varphi_j^0$ are determined by the orbital motion of the perturbing bodies and by the rotation and orbit of Mars and can be expressed as linear combinations of fundamental arguments, such as the mean longitudes of Earth, Mars, Jupiter, and Saturn, and the node of Phobos and Deimos. The main terms are related to arguments which are multiples of the mean longitude of Mars, the largest nutation being semi-annual with an amplitude of about 500 mas for the prograde component (Baland et al., 2019). The main nutation terms have first been measured by Borderies et al. (1980) with large uncertainties (at 50-100% level). Le Maistre (2013) and Le Maistre et al. (2018a) recently published new estimates of those terms with an accuracy of few tens of mas, still insufficient to constrain the core characteristics. The radioscience experiments (RISE and LaRa) will further improve the main nutation terms of Mars.

2.1.3 Polar motion

Polar motion describes differential motion between the figure and spin/AM axes. The projection of the spin axis in the BF is often denoted $(X_P, -Y_P)$ (the minus sign comes from the convention used for Earth polar motion) and can be expressed in terms of two angles as $(-\varepsilon_{PM} \sin \chi_{PM}, -\varepsilon_{PM} \cos \chi_{PM})$, with χ_{PM} and ε_{PM} , the angles from the BF to the AM frame (see Fig. 2). Forced polar motion is due to the redistribution and motion of mass elements at seasonal time scales. The existence of free oscillations, like the Chandler Wobble (CW), if excited, induce an additional component to be added to the seasonal components. Forced polar motion X_P and Y_P can therefore be expressed as series of seasonal periodic components, similarly as the variations in rotation angle of Eq. (2), with amplitudes expected to be in the range between 0 and 15 mas (Defraigne et al., 2000; Van den Acker et al., 2002) (see section 2.3). The atmosphere could also excite the CW, a normal mode for the motion of the spin axis with respect to the figure axis. The period of the Martian CW is expected to be around 200 days for the non-hydrostatic case and 220 days for the hydrostatic case (Van Hoolst et al., 2000a,b), and its amplitude could be of the order of 10 to 100 mas (Dehant et al., 2006). This amplitude can vary significantly from one year to another as has been observed on the Earth (Seitz and Schmidt, 2005). LaRa, which will be at a higher latitude than RISE, is better suited to detect Polar Motion and/or the CW (Yseboodt et al., 2017a,b). However, LaRa latitude is still not very high and the CW detection will depend on its actual amplitude.

2.1.4 The rotation matrix

The rotation matrix from the BF to the IF can be expressed in terms of the Euler angles $(\psi, \varepsilon, \phi)$ as (Reasenber and King, 1979)

$$\vec{M} = R_z(-\psi).R_x(-\varepsilon).R_z(-\phi). \quad (6)$$

More conveniently, the transformation can be performed by using the three types of rotational variations as (Folkner et al., 1997a; Konopliv et al., 2006; Le Maistre et al., 2012)

$$\vec{M} = R_z(-\psi)R_x(-\varepsilon)R_z(-\phi)R_y(X_P)R_x(Y_P) \quad (7)$$

where $(\psi, \varepsilon, \phi)$ are the AM/spin Euler angles.

2.2 Rotation and Interior structure

The time-dependent tidal forcing exerted by the Sun, the other planets, and Phobos and Deimos on the flattened Mars induces periodic nutations of its rotation axis (e.g. Dehant and Mathews, 2015). Nutations can be resonantly amplified when their frequency is close to that of a rotational normal mode, in particular the CW, the Free Core Nutation (FCN),

and the Free Inner Core Nutation (FICN). The CW is a motion of the rotation axis around the figure axis and occurs when both axes have an offset from each other. The FCN mode describes a relative rotation of the liquid core with respect to the mantle. The FICN is a relative motion of the rotation axis of a solid inner core with respect to those of the mantle and liquid core and therefore can only affect nutation if Mars has a solid inner core. The period of the three normal modes and the amplification they induce depend on the moments of inertia of the planet, core, and inner core and on their capacity to deform in response to rotation rate variations and tidal gravitational forcing (elastic deformations due to external tidal potential and rotational centrifugal potential) (e.g. Mathews et al., 1991; Dehant and Mathews, 2015).

The CW has a long period in a rotating frame tied to the planet, while the FCN and FICN, as the nutations, have nearly diurnal periods in that frame and long periods in the inertial frame. Therefore, at the first order, the influence of the CW on nutations is very small and usually neglected.

Although the resonant amplification induced by the FICN could in principle be detected by LaRa (Defraigne et al., 2003), constraints about the core composition deduced from geodesy data (Rivoldini et al., 2011; Khan et al., 2018) would require unrealistic low core temperatures (Fei et al., 2000; Plesa et al., 2016) (close to the Fe-S eutectic temperature) for inner-core formation to occur. For this reason, we do not consider Mars models with an inner core.

For a tri-axial planet with a liquid core, to first order the frequency of the CW and FCN in a frame co-rotating with Mars can be written as (Chen and Shen, 2010)

$$\omega_{\text{CW}} = \Omega \frac{A}{A_m} \sqrt{(\alpha - \tilde{\kappa})^2 - \frac{1}{4}\beta^2} \quad (8)$$

$$\omega_{\text{FCN}} = -\Omega \frac{A}{A_m} \sqrt{(\alpha_f - \tilde{\beta})^2 - \frac{1}{4}\beta_f^2} - \Omega \quad (9)$$

where Ω is the rotation frequency of Mars, A the equatorial moment of inertia, A_m the equatorial moment of inertia of the mantle, α and β are the dynamic polar and equatorial flattenings of the planet and the corresponding symbols indexed with f are those of the core. The compliance $\tilde{\kappa}$ characterizes the yielding of the planet to tidal forcing and the compliance $\tilde{\beta}$ quantifies the core's capacity to deform due to rotation rate variations (e.g. Dehant and Mathews, 2015). The dynamical polar and equatorial flattening are:

$$\alpha = \frac{C - \bar{A}}{\bar{A}} \quad , \quad \beta = \frac{B - A}{A}, \quad (10)$$

where A , B , and C are the principal moments of inertia of the planet and $\bar{A} = \frac{1}{2}(A + B)$. The dynamical flattening of the core are defined in a similar fashion.

If the planet's core equatorial flattening is small compared to its polar flattening, which is likely the case for Mars (Wieczorek et al 2019), then the frequency of the FCN can be calculated from the equation for the bi-axial case (Van Hoolst and Dehant, 2002) that is correct up to first order in flattening of the core. Corrections due to triaxiality are below 1 day in the inertial frame (Van Hoolst and Dehant, 2002) while the range of possible periods for the FCN is $[-230, -280]$ days. The FCN frequency for a bi-axial case writes

$$\omega_{\text{FCN}} = -\Omega \frac{A}{A_m} (\alpha_f - \tilde{\beta}) - \Omega. \quad (11)$$

The wobble of Mars can be calculated from the Liouville equations for a deformable planet

with a liquid core (e.g. Dehant and Mathews, 2015). By dividing this wobble with that of a rigid Mars, a *transfer function* (T_F) depending only on the interior structure of the planet is obtained. From the transfer function, the nutation of Mars can be calculated from the rigid nutation that only depends on the planet’s principal moments of inertia and on the external tidal forcing.

The prograde and retrograde nutation amplitudes \mathcal{P}' and \mathcal{R}' at a given frequency read as

$$\mathcal{P}'(\omega) = T_F(\omega)\mathcal{P}(\omega), \quad \mathcal{R}'(\omega) = T_F(-\omega)\mathcal{R}(\omega), \quad (12)$$

where \mathcal{P} and \mathcal{R} are the rigid prograde and retrograde nutations. The amplitudes and frequencies of the principal rigid nutations are given in Tab. 4. The transfer function in the frequency band of the rigid nutations can be calculated from

$$T_F(\omega) = 1 + \frac{\bar{A}_f}{\bar{A}_m} \left(1 - \frac{\tilde{\gamma}}{\alpha}\right) \frac{\omega}{\omega - \omega_{FCN}} = 1 + F \frac{\omega}{\omega - \omega_{FCN}}, \quad (13)$$

where \bar{A}_m and \bar{A}_f are the average equatorial moments of inertia of the mantle and core, ω and ω_{FCN} are frequencies with respect to the inertial frame, $\tilde{\gamma}$ describes the response of the core to tidal forcing, and F is the liquid core amplification factor. For a biaxial planet Eq. (13) is correct to first order in flattening and since this expression is not directly dependent of the dynamic flattening of the core it also provides a precise approximation for the transfer function of a triaxial planet.

2.3 Rotation and atmosphere dynamics

The exchange of angular momentum between the fluid layers and the solid planet is the main cause for the variations of the rotation of terrestrial planets in seasonal time scales (Karatekin et al., 2011). The atmospheric angular momentum variations are directly linked with the three climate cycles of Mars: CO₂, dust, and water cycles. The most important part of those variations is due to the CO₂ cycle. The atmosphere of Mars is mainly controlled by the seasonal changes in the polar icecaps, resulting from the sublimation and condensation process of CO₂. During the winter hemisphere, the temperature reaches the frost point temperature of CO₂, which condensates and creates CO₂ deposits on the surface. In return, during the summer in the same hemisphere, the CO₂ polar cap sublimates back into the atmosphere. Both H₂O ice and CO₂ ice are observed unambiguously in visible and near Infrared wavelength range (Langevin et al., 2006). Contamination of surface ices by dust can make the observations of polar caps evolution more challenging in some seasons (Langevin et al., 2007). The CO₂ and H₂O sublimation and condensation processes are related with the airborne dust. The dust in the atmosphere of Mars, alters the radiative heat transfer in the atmosphere, which then strongly affects the atmospheric circulation. The amount of dust on the surface also changes the surface albedo and thermal inertia, leading to different seasonal and diurnal surface temperature variations (Kahre and Haberle, 2010). In addition to dust, water ice clouds play an important role on the radiative balance in Mars’ atmosphere despite being a minor component of the atmosphere. Water ice clouds contribute to radiative heat transfer mainly in the infrared band, affecting the surface heat balance indirectly. It is also found that during northern hemisphere summer, the presence of water ice and dust clouds enhance the polar warming (Kahre et al., 2015). Therefore, in the frame of the present study and in view of the high level of accuracy that we will obtain the LaRa data, it is not appropriate to investigate the CO₂ cycle decoupled from the water and dust cycles, which can cause temporary variations in the CO₂ cycle. Furthermore, the seasonal and interannual variations in these cycles directly affects the zonal mean transport, or the atmospheric angular momentum in other words.

Growth and retreat of the North seasonal cap is shown to be repeatable within 1–2 degrees equivalent latitude, whereas the South seasonal cap presents noticeable variability in non-dusty years (Piqueux et al., 2015). Dust storms may have significant impact on the recession and growth rates of both polar caps. Atmospheric temperatures and dust loading are the primary source of variability in an otherwise remarkably repeatable cycle of seasonal cap growth.

Seasonal angular momentum and rotation variations of Mars estimated using the assimilated observations (i.e., reanalysis of fundamental atmospheric and surface variables) over Martian years 25 and 26 indicated that the effect of dust on Mars rotation could be visible in Mars year 25 when a global dust storm occurred (Karatekin and Montabone, 2014). The dust storm in Mars year 28 had a more significant affect on the recession and extent of caps compared to the previous dust storm (Piqueux et al., 2015). Variations in the rotation of Mars are directly related to seasonal and interannual variability of the ice caps and their observation are thus important for the understanding of Mars’ current atmospheric dynamics (Karatekin et al., 2005).

The angular momentum exchange between the surface and the atmosphere, alters the planetary rotation, causing variations up to 0.4 millisecond (or equivalently 10 m on the equator or 620 mas in terms of angular amplitude) in Martian LOD over seasonal time scales whereas the polar motion effect is predicted to be in the order of tens of milliarc-second (Karatekin et al., 2011). The predicted amplitudes of seasonal LOD variations from general circulation models with different prescribed dust scenarios as well as with assimilated observations are within the current observation uncertainties (Konopliv et al., 2011a).

3 The LaRa experiment

As explained in the introduction, the LaRa experiment uses a coherent X-band radio link to obtain two-way Doppler measurements between the Earth and the ExoMars lander on Mars. More specifically, measuring the relative position of the lander on the surface of Mars with respect to the terrestrial ground stations allows reconstructing Mars’ time-varying orientation and rotation in space, see Fig. 4.

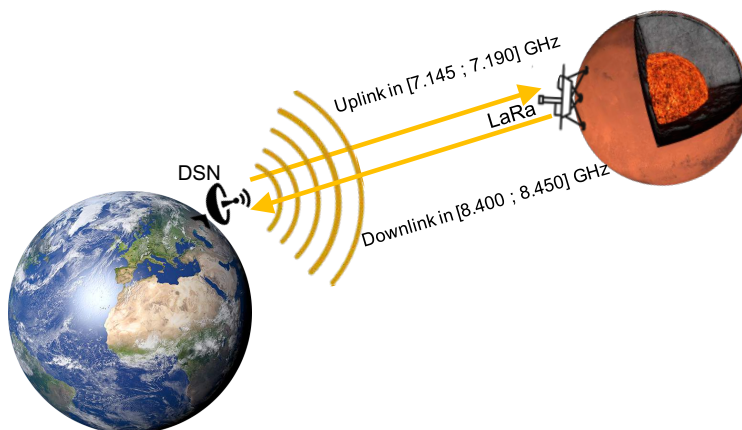


Figure 4: Representation of LaRa radiolinks between Earth and Mars.

3.1 History

The LaRa experiment is a legacy of the NETlander Ionosphere and Geodesy Experiment (NEIGE) (Barriot et al., 2001; Dehant et al., 2004). The design has changed from a three-way link lander-orbiter/orbiter-Earth to a direct-to-Earth (DTE) two-way link, and has been proposed to many missions (Harri et al., 1999; Lognonné et al., 2000; Dehant et al., 2009a; Dehant et al., 2011, 2012). At that time, we were planning to use two frequencies, UHF (Ultra High Frequency) and X-band. NEIGE was involving tracking from an orbiter and precise orbit determination (Yseboodt et al., 2003), while LaRa does not. NetLander was a proposal for a network of scientific experiments addressing the Martian geophysics. After the rejection of the mission, the experiment was proposed as part of the Geophysics and Environmental Package (GEP) for being integrated in the platform landing on Mars during the first part of the ExoMars mission to Mars in 2016. The complexity and mass budget of the platform then induced a rejection of the GEP.

Several times accepted for a pre-Phase A study, the instrument had gained enough maturity to be proposed and to be accepted on the ExoMars 2020 mission to Mars. The Announcement of Opportunity was issued on 31 March 2015 by the European Space Agency (ESA) and the Space Research Institute of the Russian Academy of Sciences (IKI RAS) for European payload. The ExoMars 2020 rover and Kazachok Surface Platform (SP) will land on the surface of Mars in March 2021. The rover will be equipped with a suite of geology and life trace seeking experiments. After the rover will have egressed, the ExoMars SP, which will contain a further suite of instruments, will begin its science mission to study the environmental and geophysical nature of the landing site, and among other goals, the atmosphere/surface volatile exchange, as well as the geophysical investigations of Mars' internal structure providing the general conditions for understanding the habitability of Mars at present and in the past. The SP and the rover take part of the 2000 kg Descent Module entry mass.

In 2015, ESA and IKI issued an Announcement of Opportunity for European payload elements on the surface platform of the ExoMars 2020 mission. The selection consisted in a technical and programmatic review of the instruments' proposal and in a thorough peer review process, performed by a Payload Review Committee, consisting of independent scientists, with competences covering the main scientific areas of the mission. The decision by the Science Programme Committee (SPC) at their meeting on 4-5 November 2015 and by the Programme Board for Human Spaceflight, Microgravity and Exploration (PB-HME) at their meeting on 17-18 November 2015, of ESA Member States selected the European payload elements on the Russian surface platform. LaRa, benefiting from a solid heritage (Technology Readiness Level 5) built on the design and breadboarding of Orban Microwave Product (OMP), was selected as part of this payload because its scientific objectives fell within the surface platform Science Priorities of the mission.

3.2 The teams and institutions

The experiment is in the hands of the Principal Investigator (PI), the scientific team, the instrument team and the Belgian authorities. The scientific team around the PI, Véronique Dehant, is mainly from Belgium, France, Russia, the Netherlands and the United States.

The instrument team is a consortium involving the Royal Observatory of Belgium (ROB) PI team, industries, and the space agencies. The main role of the ROB team in the instrument development is to ensure that the scientific requirements are respected and the science objectives will be met. The OHB company Antwerp Space is the prime contractor of LaRa, responsible for the overall project and especially for the design and manufacturing of the electronic box of LaRa. The Université Catholique de Louvain

(UCLouvain) designed the three antennas of LaRa. A series of subcontractors are also involved in the LaRa design, manufacturing and testing. The work is financially supported by the Belgian PRODEX (PROgramme for the Development of scientific EXperiments) program managed by ESA in collaboration with the Belgian Federal Science Policy Office (BELSPO). The ESA PRODEX office is closely following the LaRa project, from both managerial and technical aspects. Besides this consortium in charge of developing the instrument, BELSPO and the ESA PRODEX support the ROB team for LaRa operations and ground support. Together with ROB, ESOC (European Space Operations Centre) is involved in the preparation of the ground segment for the LaRa operations and will conduct the operations of LaRa for the entire mission duration. As prime of the Exo-Mars 2020 Kazachok Surface Platform and responsible for the science operations of it, the Space Research Institute of the Russian Academy of Sciences (IKI), the Lavochkin Scientific and Production Association and the Roscosmos State Corporation of Russia are important actors of the LaRa project. NASA will also be part of the LaRa adventure by providing tracking time on NASA's Deep Space Network (DSN) at the level of two one-hour pass per week as part of an agreement between NASA and ESA. Supplementary measurements using Planetary Radio Interferometry and Doppler Experiment (PRIDE) technique in support to LaRa will be conducted by JIVE, TU Delft in cooperation with the European VLBI Network (EVN) and other radio astronomy observatories around the world. BELSPO funds 100% of the LaRa instrument, except for the DSN and PRIDE support.

3.3 The transponder

The main element of the LaRa onboard instrumentation is the $25 \times 8 \times 8$ cm electronic transponder box. This box weights 1.5 kg while the total weight of LaRa is 2.15 kg. The transponder has two functional modes: a functioning mode referred to as a power-on mode and a sleeping mode referred to as a power-off mode. When turned on, the LaRa instrument uses at most 42 W (nominal power provided by the platform) to produce a radio frequency output power of about 5 W. LaRa will be turned on a few minutes before the expected arrival time of the uplink radio signal sent by the ground station. The receiver of the X-band RF transponder consists of an narrow-band input band-pass filter, a three-stage low-noise amplifier followed by frequency down-converters that split the required Rx gain of more than 140dB over two down-converting stages. The second intermediate frequency output is then fed to a coherent detector that compares it continuously with an internally generated crystal reference clock such that the output signal error is minimized leading to uplink signal acquisition and precise Doppler tracking. The signal enters then the heart of the LaRa transponder, namely the coherent detector. The locked signal at internal frequency is then injected in the transponder transmitter chain, which will up-convert it to the X-band output frequency. Finally, a Solid-State Power Amplifier (SSPA) amplifies the signal that will be radiated by one of the transmitting antennas (see details below). This process ensures that the output signal is coherent with the incoming signal although not at the exactly same frequency because of the 880/749 turn around ratio applied to it (as imposed by ITU, International Telecommunication Union, regulations for deep space missions (Shin, 2014)). Without a signal present at the receiver input port, the crystal oscillator is swept by a ramp generator. The transponder operates in non-coherent mode transmitting a continuous wave signal. In nominal mode, LaRa can transmit coherently (locked) and non-coherently (unlocked). The transponder contains a micro-controller unit handling the telemetry (LaRa health data) and the transponder electronics. For the sake of risk minimization, the SSPA and transmitting antenna (Tx) are redundant. The transponder is connected to the power distribution system, the thermal control system, and the SP onboard computer (so-called BIP computer). The complete

design is shown in Fig. 5.

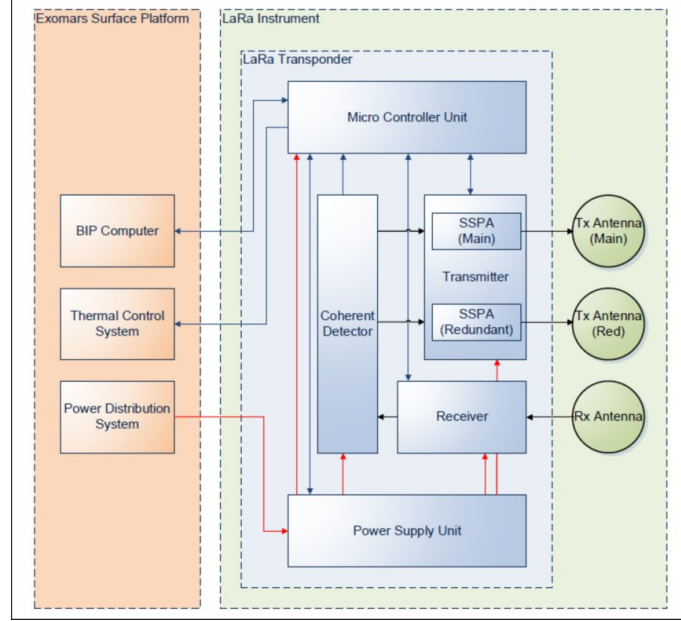


Figure 5: LaRa design of the transponder.

The design of the LaRa transponder has been finalized at the Critical Design Review (CDR) held in October 2018. The performance of the instrument has been demonstrated to be compliant with the scientific requirements. In particular, the frequency stability has been measured at different input power level (down to -148 dBm) and at different temperatures. The temperature range considered for the tests is driven by the fact that the LaRa electronics/transponder will be maintained at a temperature between -20°C and $+40^{\circ}\text{C}$ since it will be controlled by the RHU (Radioisotope Heater Unit) of the Surface Platform. The frequency stability is commonly characterized by the Allan deviation of the signal over an observation time τ . As shown in Fig. 6, the Allan deviation of all measurements are below the requirement of 10^{-13} at 60s integration time.

The functionality of LaRa has been validated using Electrical Ground Support Equipment (EGSE) facility of ESOC (see Fig. 10).

The LaRa model list allowing to meet scheduling and funding conditions is the following:

- A Structural Model (SM) for mechanical verification,
- A Thermal Model (TM) for thermal verification,
- An Electrical Interface Simulator (EIS) for electrical interfaces for SP interface verification,
- A Qualification shock model,
- Two Engineering Models (EM) for qualification and test such as radio frequency performance, SP interfaces, as well as for on-ground test model after launch,
- A Proto Flight Model (PFM) for flight that will undergo acceptance testing and some verification testing and minimum qualification testing,
- A Flight Spare kit (FS kit) consisting of PFM duplicate electronic components, and
- A Ground Support Equipment (GSE).

Some of these models and their testing are shown in Fig. 11, 12, and 13.

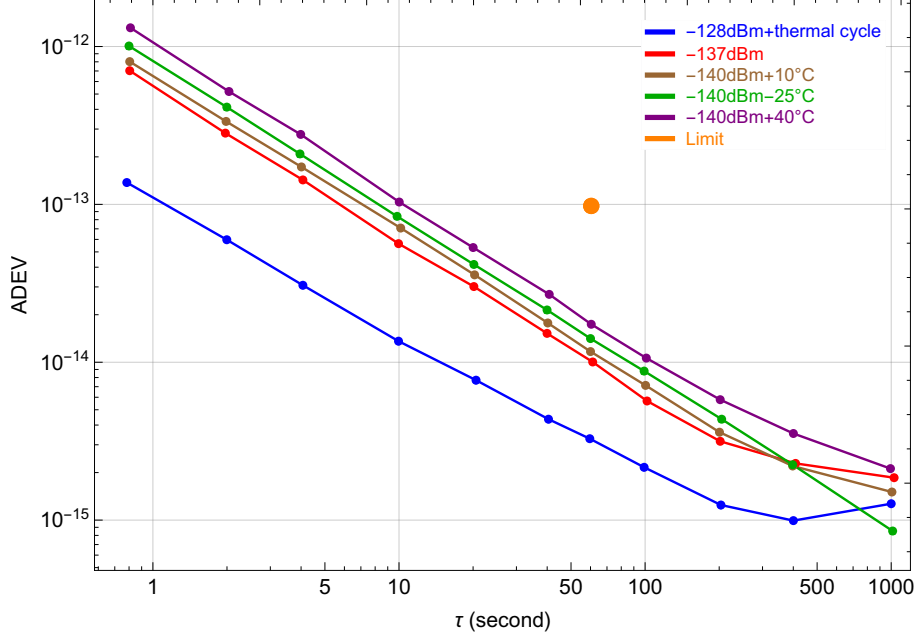


Figure 6: Allan deviation (ADEV) of the LaRa instrument computed when running at different temperatures and for different input power levels. Thermal cycle (blue) consists in a temperature variation at a rate of $10^{\circ}\text{C}/\text{h}$. The orange dot (called "limit") represents the requirement (10^{-13} at 60 seconds integration time).

3.4 The monopole antennas



Figure 7: Pictures of the receiving (Rx) (left) and transmitting (Tx) antennas (center), and Tx when ready for pattern measurement, after planetary protection process (right).

LaRa will use one antenna for receiving the signal from the Earth and two antennas (to ensure redundancy of the SSPA just prior to the transmitting antennas in the transponder output chain) for retransmitting the signal back to Earth (see detailed description of LaRa's antennas in Karki et al. (2019)). The transmitting (Tx) and receiving (Rx) antennas (see Fig. 7) operate in X-band (channel 24) around 8428.580248 MHz and 7173.871143 MHz, respectively. They radiate conical patterns with a maximum gain of about 5 dBi (antenna gain in dB w.r.t. an isotropic radiator) and a main lobe in the $[30^{\circ}, 55^{\circ}]$ range of elevation, see Fig. 8, with right-hand circular polarization. This allows a good link budget with the Earth, over its path in Martian sky. The observed effective patterns are shown in Fig. 9 (see also Karki et al. (2019)). Gamma-shaped parasitic elements surround the centrally fed monopole. They protrude from an aluminum housing, which also includes a choke ring, intended to cut edge currents and reduce the back-lobes (see Fig. 12, top-left). The Tx and Rx antenna diameters are 66 and 80 mm, and their masses are 132 and 162 g, respectively. A radome also covers the whole structure. The radiator

itself is made of a monopole fed through a square-coaxial transmission line. The latter is fed from the side of the aluminium housing. The shape of the parasitic elements controls the circular polarization purity.

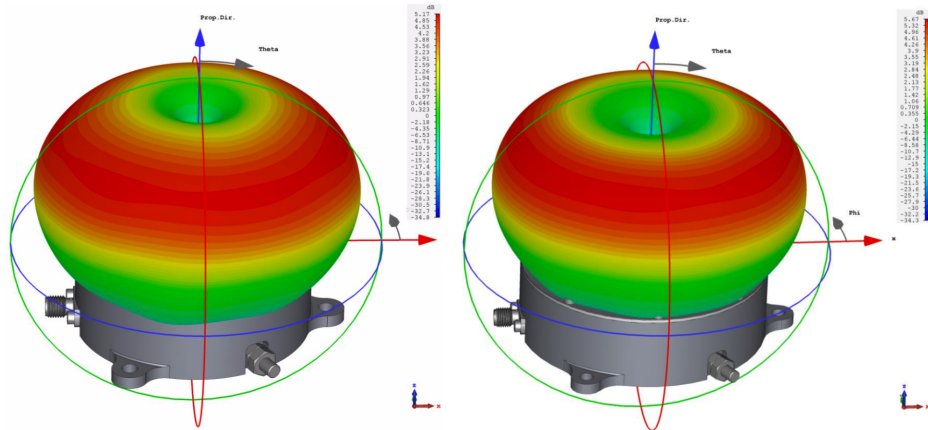


Figure 8: Computed radiation Pattern (3D) of the Rx (left) and Tx (right) antennas, above aluminium housing.

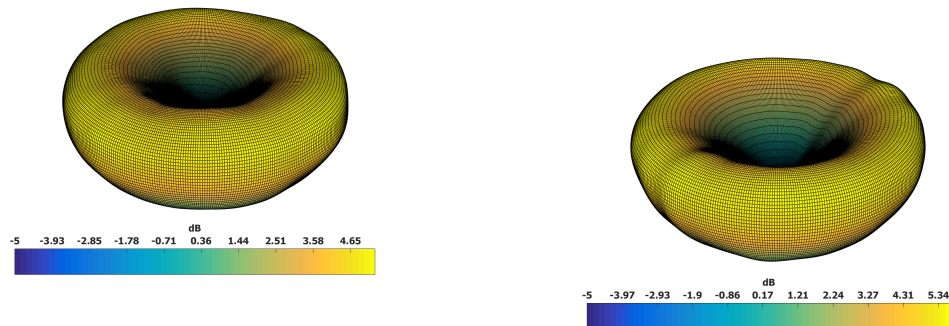


Figure 9: Observed radiation Pattern (3D) of the Rx (left) and Tx (right) antennas. Small ripples in the Tx pattern are probably due to scattering by a feeding cable

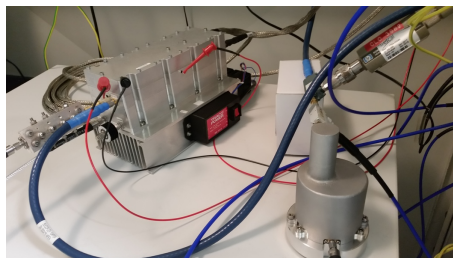


Figure 10: Photo of the end-to-end testing at ESOC (European Space Operations Centre, in Darmstadt, Germany) of the Engineering Models of the Electronic box (E-box, transponder part) and test caps containing the antennas.

Unlike the LaRa electronic box, the antennas will not be mounted on a thermally controlled panel and will therefore experience a larger range of environmental temperatures, between -120°C and $+60^{\circ}\text{C}$. As a result, a dedicated qualification campaign for materials

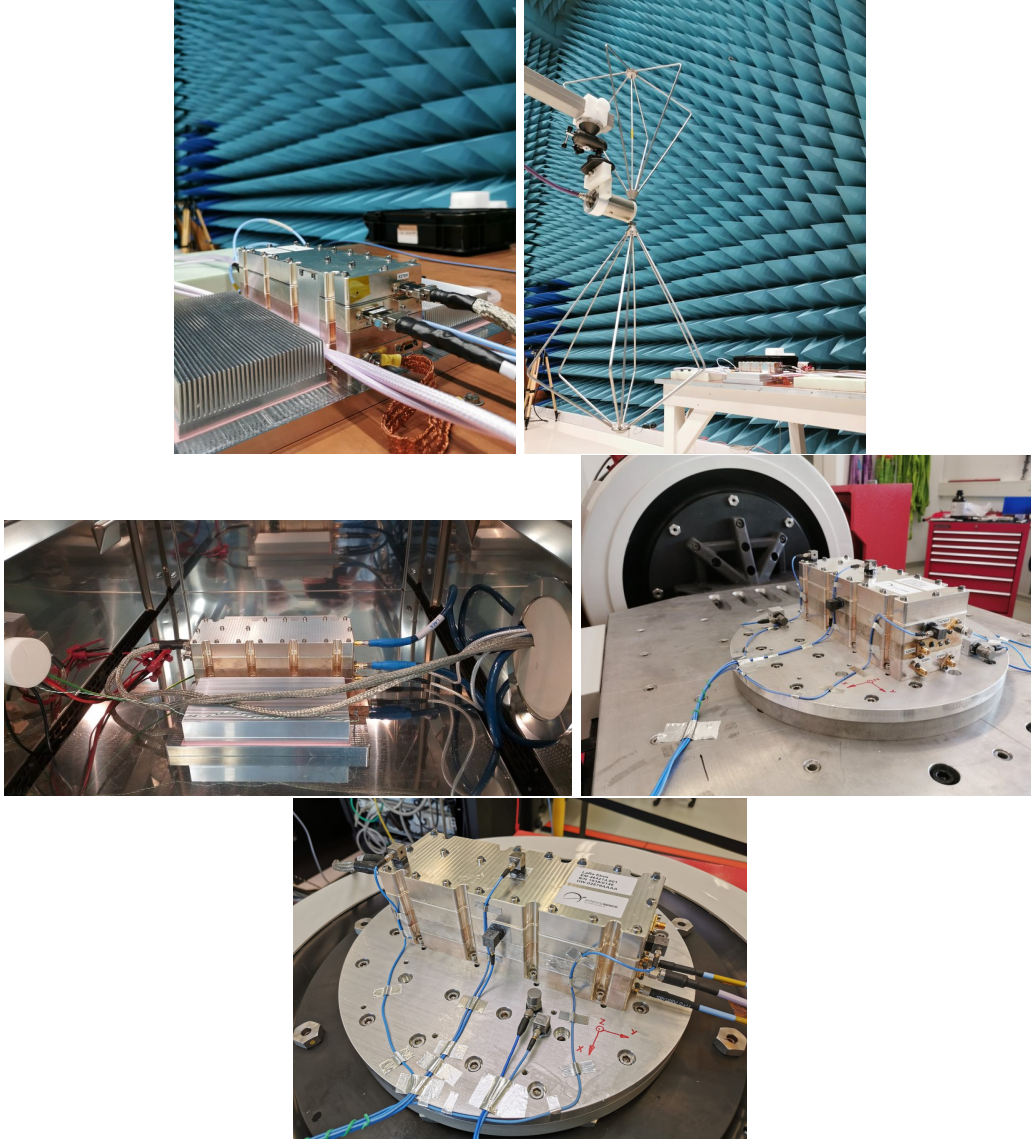


Figure 11: Top-left: flight model of the transponder during EMC testing. Top-right: EMC facility. Medium-left: flight model of the transponder in a thermally-controlled chamber when testing at AntwerpSpace; the e-box is in the back of the chamber. Medium-right: flight model of the transponder during vibration tests. Bottom: flight model of the transponder just before entering TVAC chamber.

and process used for these antennas had to be carried out. The fully metallic design of the radiator itself enables withstanding the huge temperature range.

The RF harness, i.e. coaxial cables linking the antennas to the transponder box, are about 2 m long, inducing a 1.7 dB power loss in the link-budget (see below).

3.5 The ground segment

The LaRa experiment involves a space segment, which is the LaRa instrument itself (i.e., transponder and receiving/transmitting antennas), as well as a ground segment consisting in three potential networks of large antennas distributed around the globe. The chosen nominal one is the NASA Deep Space Network (DSN) that consists of three deep-space communications facilities placed approximately 120 degrees apart in longitude: (1) at Goldstone, in California's Mojave Desert, USA; (2) at Robledo near Madrid, Spain;

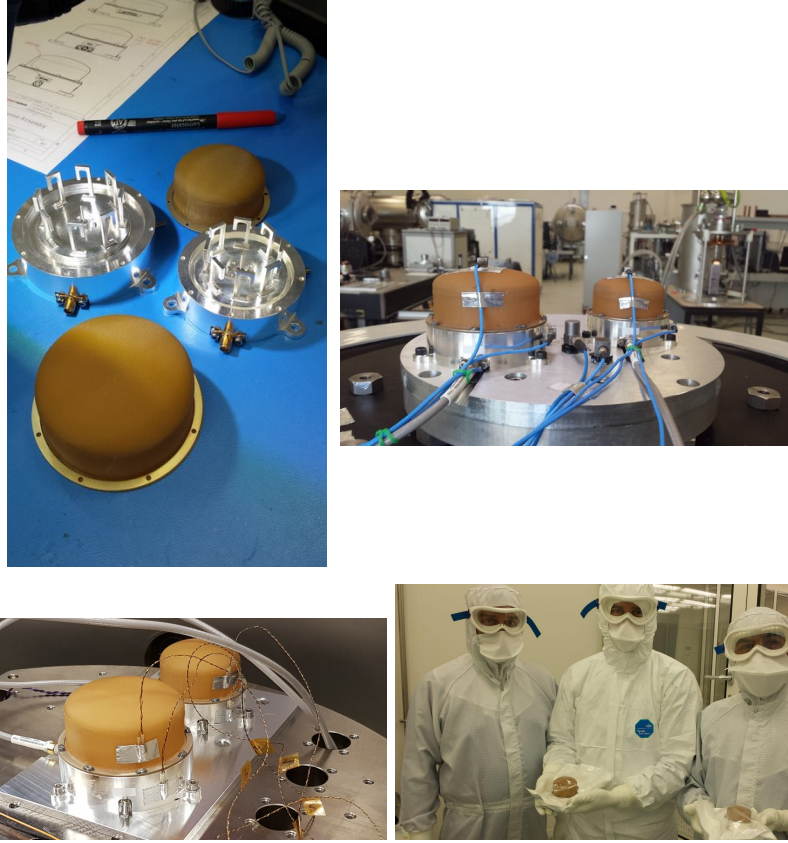


Figure 12: Top-left: flight model of the antennas open to show the parasitic form of the antennas. Top-right: flight models of antennas during vibration tests. Bottom-right: flight models of antennas before entering TVAC chamber. Bottom-right: flight models of antennas in the hands of the responsible engineers.

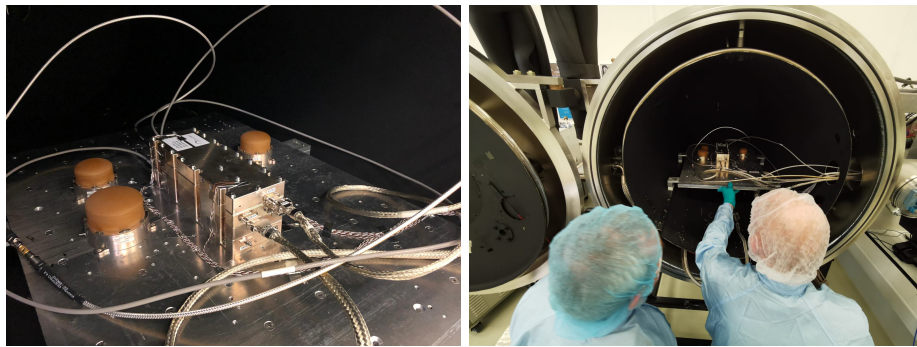


Figure 13: Photos of the flight models of the antennas and transponder entering the TVAC testing.

and (3) at Tidbinbilla near Canberra, Australia. Each of these facilities includes several 34 m antennas and one 70 m antenna. The 70 m DSN antennas are baseline for LaRa ground segment as only these are currently able to track the weak signal transponded by LaRa during a whole Martian year (see next subsections).

As backup solution, when the Earth-Mars distance is basically smaller than 1.5–2 astronomical units (AU), the LaRa experiment foresees to also use the 35 m antennas of the ESA's ESTRACK network. ESTRACK stations are located in Cebreros near Madrid, Spain; in New Norcia, Australia; and near Malargúe, Argentina.

The Russian Ground Station (RGS) network might also be used to track LaRa provided

some major upgrades of the RGS antennas are performed. The network consists of two 64 m antennas in Bear Lakes near Moscow and Kalyazin in Tver area, and a 70 m antenna in Ussuriisk, north of Vladivostok. Unlike the other two networks, the Russian antennas are all located in the northern hemisphere within a limited range of longitudes of about 90° , which makes them much less convenient for the experiment during an entire Martian year. Indeed Mars barely rises above 10° elevation in the RGS sky during several consecutive weeks (about 30 weeks below 30° elevation) every Martian year. As shown in the next section, this has a strong impact on the link budget because of the large atmospheric losses at low elevation angle and the absence of global coverage in the antenna positions (only in Russia). For these reasons, these ground stations are disregarded at this point of the project.

All ground stations mentioned above are equipped with ultra-stable hydrogen maser local oscillators (LO) ensuring the highest reference frequency stability.

In addition to the space agencies' deep space tracking networks, a global network of radio telescopes equipped with Very Long Baseline Interferometry (VLBI) instrumentation has the potential of providing useful measurements for the LaRa experiment. About forty VLBI radio telescope antennas ranging in diameters from 220 m (the illuminated diameter of the Arecibo radio telescope) to about 20 m are distributed over all continents. These telescopes can operate using the PRIDE technique for obtaining Doppler measurements for LaRa in both the nominal two-way coherent regime and in the non-coherent free-running regime. The former case represents a so called 'three-way' configuration (up- and downlink from/to a ground station plus a one-way downlink from SP to a radio telescope) or a one-way – just a downlink to a radio telescope in a free-running mode.

3.6 The link budget

For the design of a radioscience experiment like LaRa, the link budget is an important aspect to be analysed in order to ensure the acquisition of Doppler measurements at the Earth ground stations. Based on the performance of the LaRa instrument itself, and on the performance of the receiving and transmitting ground stations, the uplink signal level received at the LaRa receiving antenna (Rx) and the signal-to-noise ratio (SNR) expected at the Earth stations can be computed, while accounting for the propagation medium in the frequency band of interest (X-band). These two quantities are shown in Fig. 14 for four Earth years as a function of time or equivalently Earth-Mars distance, and for the different ground stations.

The LaRa transponder has been designed to lock and maintain the lock for more than one hour on an uplink signal level down to -140 dBm. As shown on the left panel of Fig. 14, the LaRa receiver chain ensures the tracking of the DSN-70 m uplink signal at any time during the next two Martian years. Fig. 14 right panel, shows the SNR margin at the ground station receiver inputs for the 70 m DSN antennas (orange), the 35 m ESTRACK antennas (red) and the 64 m RGS antennas (blue). When the curves are below zero, the lock can not be maintained anymore in the closed-loop mode and, if the uplink is guaranteed, tracking in open-loop mode has to be performed, i.e. instead of using the ground station receiver PLL (Phase-Locked Loop) that directly provides the Doppler, we need to record the whole signal returning back from Mars in a certain frequency band after being transponded at Mars with the classical deep-space transponder ratio (880/749) and reconstruct the Doppler afterwards (see also Section 3.7.1). As clearly shown on this panel, DSN antennas (baseline for LaRa) can always track LaRa's signal while the other two can only be used below a certain distance (1.5-2 AU for both RGS and ESTRACK stations). The RGS computation has been performed assuming Bear Lakes antenna performance and location. As mentioned in the previous section, the SNR drops significantly when Mars stays at elevation lower than 30° in Bear Lakes' sky due to atmospheric losses

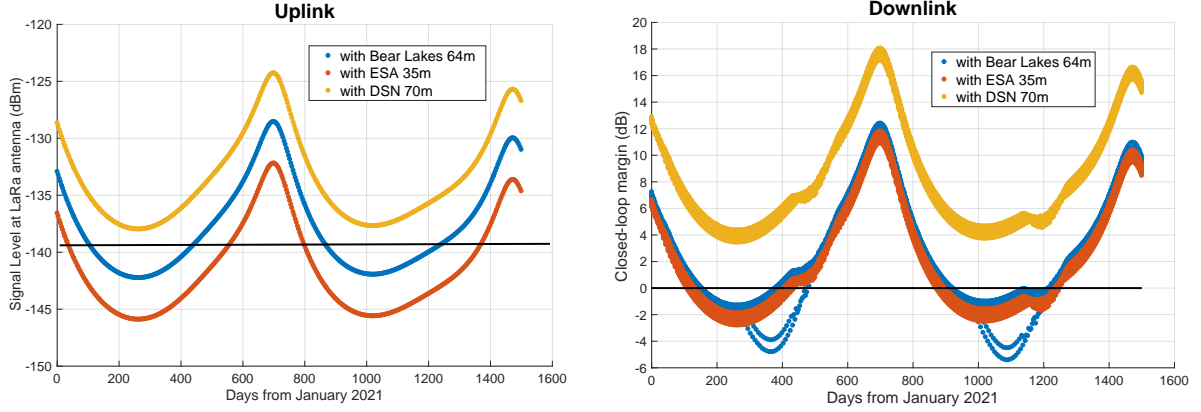


Figure 14: LaRa uplink signal level at Rx antenna (left) (which includes cable loss and antenna gain) and SNR margin for closed-loop tracking of LaRa’s downlink signal (right). The black lines indicate the lower limit above which the signal can be locked at the LaRa antenna (left) or at the ground station (right).

(see large deflections in blue curve of Fig. 14 right panel around 350 and 1100 days). In addition, the link-budget is computed in a worst-case scenario where the SP would be tilted 20° Northwards. Then, the Earth would sometimes not rise above 25° - 30° in LaRa’s sky, forcing to track at lower elevation at Mars and therefore with lower LaRa antennas gain as suggested by Fig. 8. This is responsible for the slight distortions observed in the downlink margins of each of the three stations around 500 days and 1200 days (see Fig. 14 right panel).

As a conclusion, based on the link-budget analysis, we demonstrate that the LaRa experiment is well designed for an actual measurement recording in closed-loop mode with DSN (see Section 3.7.1 for the complete explanation).

It must be mentioned that, for the downlink (not shown here), it is always possible to observe in open-loop mode (still in two-way configuration) with any of the above-mentioned networks, if the uplink is working. The limitation of the use of the ESTRACK stations and the Russian ground stations, is arising from the uplink budget when the LaRa transponder is not able to lock on the signal uplink. If the uplink uses a better emission performing station like some of the DSN 34 m antennas (not shown in Fig. 14), the link can be closed in the open-loop configuration.

3.7 The measurements

The LaRa measurements are two-way Doppler shifts acquired directly at the Earth ground stations. No data are stored onboard the platform except for a few LaRa health measurements such as internal temperatures and voltages of different components. These data are transmitted to Earth via the telemetry of the platform.

3.7.1 Data types

Ground Station Doppler data The ground tracking stations are equipped with PLL receivers making the tracking of Doppler-induced changes in frequency of the X-band downlink received carrier possible. These receivers generate a model of the received signal and cross-correlate the model with samples of the incoming downlink signal. They use a PLL to estimate the difference; that PLL estimate plus the model is the measurement. PLL receivers allow signal acquisition, lock-up, and detection in real time (Morabito and

Asmar, 1994). The closed-loop data are delivered in various format (*e.g.* ATDF, ODF, TNF, TDM, etc.). Among the quantities on a tracking file are measurement acquisition time, Doppler shift, Doppler counts and Doppler reference frequencies either in the form of a constant frequency or uplink ramps. LaRa experiment will nominally perform tracking in the closed-loop mode. The LaRa transponder is designed to obtain closed-loop two-way Doppler measurements at the accuracy level (see Table 2 for the details on the link budget) of 0.05 mm/s at 60 second integration time (or equivalently 2.8 mHz). Nevertheless, at long Earth-Mars distance, the signal-to-noise level at the ground stations will be so low that lock on the downlink carrier could be jeopardized and measurements acquisition might have to be performed in open-loop mode (this will be the case only if DSN 70 m antennas are not available, see the previous section). The open-loop system mixes an incoming intermediate frequency signal with a signal whose frequency is a linear approximation of the predicted frequency. The baseband signal is passed through a filter whose bandpass is centered at the expected frequency and has a sufficiently wide bandwidth to allow for any unexpected signal frequency excursions. A set of analog-to-digital converters digitizes the received bandwidth and then writes the samples onto open-loop data files. The (non-real time) processing of open-loop data basically consists of performing signal detection on the recorded samples using high accuracy signal parameter estimation algorithms. The received sky frequencies are then reconstructed from the detected frequencies. This method is used for very noisy signal for low SNR, but, as mentioned above, the limitation is not arising from the downlink SNR but rather from the uplink. It will not be necessary to use the open-loop method for the LaRa experiment.

3.7.2 The error-budget

The precision of the Doppler measurements for LaRa is limited by disturbing effects. Non-signal disturbances in a Doppler link are mainly due to (Asmar et al., 2005):

- The instrumental noises (random errors introduced by the ground station or LaRa),
- The propagation noises (random frequency/phase fluctuations caused by refractive index fluctuations along the line-of-sight),
- Systematic errors (*e.g.* ground station delay uncertainty).

Instrumental noises include phase fluctuations associated with finite signal-to-noise ratio (SNR) on the radio links, ground and LaRa electronics noise, frequency standard noise, and antenna mechanical noise (unmodeled phase variation within the ground station) (*e.g.* Dehant et al., 2009b). The larger contribution to the instrumental noise is the thermal noise that is related to the mean antenna system operating noise temperature. The propagation loss will vary as a function of the distance between Mars and the Earth. The thermal noise is of the order of 10^{-2} mm/s at 60-s for LaRa.

The propagation noise perturbs both the uplink and the downlink. It is caused by phase scintillation as the deep space wave passes through media with random refractive index fluctuations such as solar plasma, Earth and Mars troposphere or ionosphere (Asmar et al., 2005; Zuber et al., 2007; Bergeot et al., 2019). The plasma Doppler shift is induced by all the charged particles along the radio wave path and depends on the elongation. Thus, the observations should be performed at times far from solar conjunction to avoid the solar plasma effects. A model adapted to Doppler data exists to estimate the standard deviation (accounting for the two-way link) due to solar phase scintillations in the range $5^\circ \leq \text{elongation angle} \leq 27^\circ$ (see Zuber et al. (2007) and reference therein).

The Earth's ionosphere induces a frequency shift which can be partly removed by using models like, for example, the Klobuchar model (Klobuchar, 1987).

Unlike the ionosphere, the troposphere (neutral atmosphere) is a non-dispersive medium, thus the propagation delay is not frequency-dependent. The total delay of radio signal caused by the neutral atmosphere depends on the refractivity along the traveled path, itself depending on pressure and temperature. There are two components: the dry component and the water vapor (the wet component). At X-band frequencies, tropospheric effects dominate the Doppler error with respect to ionospheric and solar plasma errors except for elongation smaller than $10\text{--}15^\circ$ when the latter becomes dominant (e.g. Pätzold et al., 2016; Le Maistre et al., 2019). The tropospheric delay due to dry air corresponds to 90% of the tropospheric effect. It depends mainly on well-known atmospheric pressure and temperature on the Earth’s surface and therefore it is easy to account for it from a model. The unmodeled remaining 10% of total tropospheric delay due to the wet component depends on the water vapor content of the Earth’s atmosphere in the propagation path, mainly below altitudes of 8–15 km (e.g. Zuber et al., 2007). This component is difficult to model without measurements due to the high spatial and temporal variability of the water vapor. However, the use of GNSS data or products will help to decrease the wet troposphere contamination of the observation (Feltens et al., 2018). Finally, the ground station contributes to Doppler noise due to temperature and location uncertainties.

The order of magnitude of Mars’ ionosphere effects have been determined by Bergeot et al. (2019) from the subsurface mode of the Mars Express MARSIS radar. Bergeot et al. (2019) developed also an empirical model of the Mars’ ionosphere called MoMo (MOdel of Mars iOnosphere). It is based on the large database of Total Electron Content (TEC) derived from the subsurface mode of MARSIS. The model provides the vertical TEC as a function of solar zenith angle, solar activity, solar longitude and the location. MoMo shows that Mars’ ionosphere variability is mainly driven by the solar illumination and activity, and the seasons, with amplitude variations of the $v\text{TEC}$ over an entire day lower than 2 TEC_u . MoMo was used to estimate the impact on Doppler radioscience. At X-band, the maximum Doppler shift was estimated at the level of 0.05 mHz, or 0.001 mm/s, which is almost negligible but better to be estimated, in particular in view of the time variations of this correction.

The order of magnitude of the effects of the Martian troposphere on the Doppler signal has been estimated at a level near the Doppler instrument noise level. It can be estimated/calibrated using surface pressure and temperature measurements by the surface platform. This noise is well below the noise due to Earth water vapor fluctuations (Folkner et al., 2018).

All error contributions and their levels have been quantified, using the results from Zuber et al. (2007) as reference. Table 2 shows the LaRa error budget on the two-way Doppler, assuming uncalibrated solar plasma and wet tropospheric effects as well as large ground station noise (probably too large as the dynamics on the radio signal from an orbiter is larger than that on a lander). Outside of the extreme cases (but still quite conservative), the RSS (Root Sum Square) value reported in this table is about 0.07 mm/s@60s. The RMS (Root Mean Square) value reported in this table is of the order of 0.03 mm/s @60 s or maximum 0.05 mm/s @60 s (equal to 2.8 mHz@60s in X-band) considered as representative noise level of LaRa measurements and used in the simulations shown below or in the companion papers (Le Maistre et al., 2019; Péters et al., 2019).

3.7.3 MOP signatures in LaRa’s measurements

The sensitivity of the LaRa DTE Doppler measurements to the direction of the Martian spin axis, and hence to nutation is reduced when the Earth declination (the angle between the Mars-Earth vector and the Martian equatorial plane) is close to zero (Yseboodt et al., 2017a) because the Martian rotation axis is then perpendicular to the line-of-sight. The geometry of the mission and in particular, the evolution of the distance between Earth

Table 2: Contributions to Doppler measurements errors for LaRa two-way X-band radio link integrated over 60 seconds.

Error source	Two-way Doppler noise level (mm/s)
Instrumental LaRa noise and thermal noise at ground station	<0.03
Solar plasma effects at 10° and 25° elongation (Zuber et al., 2007)	0.10 and 0.03
Earth Ionospheric effects (including scintillations)	0.02
Tropospheric effects of the Earth atmosphere wet component at 30° elevation angle (dry contribution is assumed properly corrected from pressure and temperature) or dry atmosphere	0.06 or <0.03
Mars Ionospheric and tropospheric effects	<0.03
Ground station	0.04
Total Root Sum Square (RSS, computed as the square-root of the sum of the above square noise values)	0.13 and 0.07
Total Root Mean Square (RMS, computed as the square-root of the mean of the sum of the above square noise values)	0.05 and 0.03

and Mars and the evolution of the Earth declination are shown in Fig. 15.

Since the Doppler observable is, to the first order, the projection of the lander velocity on the line-of-sight, a motion of the spin axis in space when the declination is close to zero results in a negligible contribution in the Doppler signal.

Table 3: Maximal value of the MOP signature in the Doppler observable (in mm/s) for the ExoMars 2020 mission. The nominal mission time interval is used. The lander position is in Oxia Planum (18.20° N latitude, 335.45° E longitude). See Folkner et al. (2018), Section 2, and Table 4 for a description of the MOP model and the numerical values used.

MOP	MOP signature (mm/s)
Nutations in obliquity $\Delta\epsilon$	0.223
Nutations in longitude $\Delta\psi$	0.253
Large liquid core ($T_{FCN} = -242$ d)	0.008
Small liquid core ($T_{FCN} = -285$ d)	0.004
Precession ($\Delta\dot{\psi}_0 = 2$ mas/y)	0.051
LOD variations	0.574
Polar motion	0.024

The maximum values of the rotation angles signatures in the Doppler observable are given in Table 3. The liquid core signature is computed assuming a Free Core Nutation (FCN) period of -242 days for a large liquid core or -285 days for a small liquid core. The largest signatures (up to 0.57 mm/s) are due to the Length-of-day (LOD) and the rigid nutation because they induce a large effect on the lander displacement (larger than 10 meters on Mars surface). The effects of the polar motion and of the liquid core in the Doppler signal are one or 2 orders of magnitude smaller (maximum 0.02 mm/s) for a lander with a 18° latitude like ExoMars-2020.

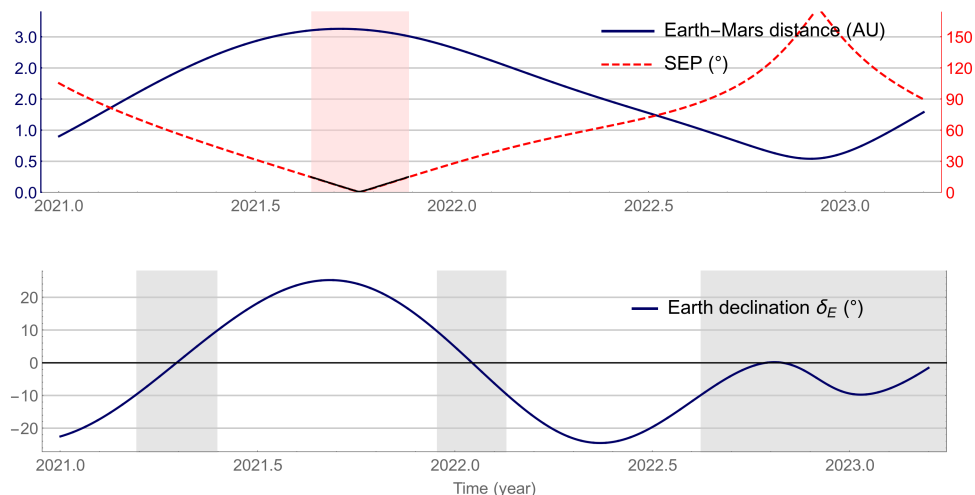


Figure 15: Evolution of the Earth-Mars distance and the Earth declination as a function of the mission timing.

3.8 PRIDE measurements

Planetary Radio Interferometry and Doppler Experiment (PRIDE) has been developed at the Joint Institute for VLBI ERIC in collaboration with the Delft University of Technology and other partners. It is designed as an enhancement of planetary science missions' radioscience suite. The essence of PRIDE is in applying hardware and data handling algorithms developed for high-resolution radio astronomy studies of galactic and extragalactic objects using Very Long Baseline Interferometry (VLBI). In applications to interplanetary spacecraft as targets, VLBI observations must be treated in the so called near-field VLBI mode. This mode takes into account that the wave front of radio emission generated by spacecraft within Solar system arrives to Earth with non-negligible curvature (spherical in zero approximation) unlike the case of galactic and extragalactic sources, for which the wave front can be treated as planar. The main measurables of PRIDE are lateral coordinates of the target (radio emitting spacecraft) defined in the celestial reference frame (typically - the International Celestial Reference Frame, currently – ICRF-3, as defined by the International Astronomical Union) and radial velocity of the target. The latter is deduced from Doppler measurements.

The general methodology of PRIDE is described in (Duev et al., 2012) and specific details for Doppler extraction from PRIDE measurements in (Bocanegra-Bahamón et al., 2018). To date, PRIDE was demonstrated in observations of the ESA's Mars Express (Duev et al., 2016; Molera Calvés et al., 2017) and Venus Express (Bocanegra-Bahamón et al., 2019). As demonstrated in multiple observations of Mars Express, PRIDE can achieve Doppler measurements in a three-way regime with the median noise level of ~ 2 mHz (0.03 mm/s) in 10 s integration or ~ 0.013 mm/s in 60 s integration (Duev et al., 2016). PRIDE is adopted as one of eleven experiments of the ESA's flagship mission JUICE (Jupiter Icy moons Explorer) scheduled for launch in 2022 (Witasse et al., 2015).

In the LaRa context, we intend to use PRIDE as a supplementary technique, by no means replacing the nominal two-way radio measurements conducted by DSN facilities. However, as demonstrated recently in observations of *e.g.*, ESA's Venus Express, due to a wider choice of ground-based receiving stations among PRIDE radio telescopes, some of them, at a particular time, might be in a more favorable position (a higher elevation of a target, a better seasonal climatic conditions, a less turbulent patch of ionosphere over the ground antenna, etc.) for achieving Doppler measurements with a very low noise (see, *e.g.*,

Fig. 6 in (Bocanegra-Bahamón et al., 2019)), lower than a single nominal dedicated DSN or ESTRACK facility. This simple PRIDE advantage might help to achieve the science goals of LaRa.

The Doppler measurements extracted from PRIDE observations contain the same information of interest as contained in the measurements recorded at DSN but they are statistically independent from those nominal measurements in noise contributions defined by the downlink propagation and ground receiving instrumentation. Thus, we intend to conduct PRIDE measurements in parallel with nominal two-way LaRa radio sessions. A detailed error propagation analysis in PRIDE measurements is given in Section 3.3 of Bocanegra-Bahamón et al. (2019). We note that the overall setup of the nominal two-way configuration of LaRa experiment is essentially the same as in Venus Express observations described by Bocanegra-Bahamón et al. (2019), thus making the mentioned error propagation directly applicable to the LaRa case. However, in the months prior to LaRa operations we intend to conduct special verification PRIDE observations of operational Mars landers and orbiters in order to tune up observational setup and data processing algorithms.

In addition, PRIDE might be exercised in one-way (downlink only) radio sessions. The contribution of PRIDE measurements in this non-coherent (one-way) regime is at least in providing test and calibration information. This one-way regime will be investigated further in the months preceding the ExoMars mission launch.

3.9 LaRa operations

After landing, the measurements will be carried out twice per week during the whole mission lifetime (twice per week during the minimum guaranteed mission of one Earth year and during the extended mission, with a possible relaxation to once per week during lander hibernation seasons if any). No operation will be done at solar conjunction and for a solar elongation angle lower than 5° and special care (such as avoiding solar irruption period) will have to be performed at solar elongation angle between 5° and 10° . Each tracking session will last one hour and will be performed during the local day time at Mars because of power-availability on the lander. LaRa is designed to allow communication with the Earth when the line-of-sight to the ground station is between $30^\circ - 55^\circ$ of elevation. Nevertheless, we plan to operate LaRa preferably when the Earth appears between 35° and 45° of elevation above the lander's horizon because (1) this is the elevation range of LaRa antennas best gain (see Fig. 8), (2) this limits Mars atmospheric effects and problems related to local reflections of the signal and local topography blocking the view to the Earth, (3) this is the elevation range of best sensitivity to the nutation parameters (Le Maistre et al., 2019). First tracking session of each week will be performed from lander's east direction (Earth rise) and second one from lander's west direction (Earth set), or *vice versa*, the first tracking session of each week can be performed from lander's west direction (Earth set) and second one from lander's east direction (Earth rise) as it is important to alternate the line-of-sight azimuth direction from one pass to the other (Le Maistre et al., 2019). Earth tracking stations to be used will be preferably those that have low water content in the atmosphere, reducing Earth tropospheric disturbances. Additional constraints on LaRa operations from other units of the SP (system and scientific payload) are expected to avoid inter-units interference. For instance, LaRa will certainly not operate simultaneously with the Ultra High Frequency (UHF) transponder used for Telemetry and Telecommand (TM/TC) communications with Martian orbiters. LaRa will also have to wait for ExoMars rover egress before starting to operate for possible interference reasons.

4 LaRa expected results

4.1 MOP determination

We carry out numerical simulations with the GINS (Géodésie par Intégrations Numériques Simultanées) software in order to assess the uncertainties with which LaRa will allow to determine the Mars Orientation and rotation Parameters (MOP) as well as the lander coordinates at the surface of Mars. The actual rotation model used to create the synthetic Doppler data is classical and described in details in Le Maistre et al. (2018b). Basically, the angles at epoch $(\varepsilon_0, \psi_0, \phi_0)$, rates $(\dot{\varepsilon}_0, \dot{\psi}_0, \dot{\phi}_0)$ and spin angle variation amplitudes $(\phi_m^{c/s})$ are from Konopliv et al. (2016). The amplitudes of the truth model of nutation are computed from the model of rigid nutation of Roosbeek (1999) or Baland et al. (2019), modulated by a liquid core of FCN period equal to -240 days and of amplification factor F equal to 0.07. The CW amplitudes are arbitrarily chosen and its period is fixed (and not estimated) to be around 200 days for the non-hydrostatic case and 220 days for the hydrostatic case. The numerical values of the MOP that are estimated are reported in Tab. 4 along with the post-fit uncertainties for seven different scenarios:

- sol1: This is the solution obtained after one Earth year of data accumulation (ExoMars 2020 nominal mission). The nutation parameters estimated here are the amplitudes of the complex prograde (p_m) and retrograde (r_m) nutation terms at the forcing period $m = 2$ and $m = 3$, corresponding to the semi-annual period of 343.5 days and the ter-annual period of 229 days, respectively. Obliquity rate ($\dot{\varepsilon}_0$) and precession rate ($\dot{\psi}_0$) of the spin axis at epoch J2000 are estimated as well as the annual ($\phi_1^{c/s}$) and semi-annual ($\phi_2^{c/s}$) amplitudes of the Mars spin angle. See details on this setting in Le Maistre et al. (2018b).
- sol2: This solution has the same settings as sol1 parameter-wise, but is computed over one Martian year (~ 700 days corresponding to LaRa nominal lifetime).
- sol3: This solution is similar to sol2, but the annual amplitudes of nutation (p_1, r_1) are also estimated.
- sol4: This solution is similar to sol2, but the spin angle amplitudes of the ter-annual ($\phi_3^{c/s}$) and quater-annual ($\phi_4^{c/s}$) periods are also estimated.
- sol5: This solution is similar to sol2, but the nutation parameters estimated are the parameters of the nutation transfer function: F and T_{FCN} (and no more the amplitudes of the nutation series).
- sol6: This solution is similar to sol2, but the amplitudes of the CW are also estimated.
- sol7: This solution is similar to sol3 (parameter-wise), but is obtained by combining one Mars year of RISE (InSight) Doppler data together with one Mars year of LaRa Doppler data. See details on this scenario in Péters et al. (2019).

Generally speaking, we see from Tab. 4 that LaRa will allow us to determine the nutation signal very precisely, with only a few mas of uncertainty on the amplitudes and about 4 days on the FCN period. If the latter estimation is actually depending on the parameter setup, i.e. the a priori value taken for T_{FCN} (here -240 days), the former is not. One can thus confidently claim that the two most-interesting parameters, p_2 and r_3 , will be estimated by LaRa alone with 4-7 mas and 4-8 mas of uncertainty, respectively (depending on the set of estimated parameters, and for the LaRa nominal lifetime). One could even reduce those uncertainty ranges by about 2 mas if we use RISE and LaRa data together.

Such an apparently small difference in the nutation estimate uncertainties can significantly enhance the scientific return of those two missions as shown in the following section and further discussed in Péters et al. (2019). Spin angle variations and precession rate (-7608.3 ± 2.1 mas/year) are already accurately known thanks to historical lander, rover and orbiter data (Kuchynka et al., 2014; Konopliv et al., 2016), but LaRa shall definitely further improve the determination of those parameters. The precession uncertainty shall decrease from 2.1 to 0.3 mas/year. This will allow us to get one order of magnitude better on the moment of inertia of the whole planet (presently at the level of 0.3638 ± 0.0001), which is one of the main parameters that constrain the interior models (Rivoldini et al., 2011). One major discovery of LaRa could be the first-time direct measurement of the Chandler wobble amplitudes as shown in sol6. Forced polar motion in the Earth system is superposed by free oscillations of the Earth, i.e. CW. As the CW is a resonance oscillation of the planet, potential excitation mechanisms require energy in a band close to the CW frequency in order to sustain the free polar motion and thus to counteract its damping. On the Earth the CW is excited by a combined effect of atmosphere and ocean. If this free mode exist on Mars, it would provide novel information on Mars’ atmospheric dynamics in a band close to the CW frequency. Because of their low latitudes, none of the previous landed missions have been able to detect this signal, neither will the near-equatorial In-Sight mission. The detection of the CW frequency with LaRa will put some constraints on the interior of Mars, while the estimation of the amplitude will put constraints on the dissipation inside Mars, as well as on the energy in the atmosphere near the CW frequency.

Finally, because of the high accuracy of LaRa and RISE forthcoming data, one could expect that the tidal Love number h_2 , characterizing the radial deformation of Mars in response to tidal forcing, could be measured for the first time. Additional simulations (not shown in Tab. 4) show that h_2 can be estimated from LaRa alone with an uncertainty of 0.6 while a combination of RISE and LaRa data would allow estimating h_2 with an uncertainty of 0.2. This is respectively three times and one time the expected value for h_2 (Van Hoolst et al., 2003), which makes the determination of this parameter with RISE or LaRa not relevant.

4.2 Mars interior structure and atmosphere

4.2.1 Constraints on the interior of Mars

In order to illustrate and quantify how the interior structure of Mars affects its wobble and nutation we calculate the FCN period and the amplification effects on the largest nutations (retrograde annual, semi-annual, and ter-annual and prograde semi-annual) for a large set of plausible Mars interior structure models.

These interior models are built in two steps. First, we assume that the planet is spherical, isotropic, elastic, non-rotating, and in hydrostatic equilibrium. The planet has a crust that is modeled by its thickness and density, a silicate mantle, and a fluid and iron-sulfur core. The range of densities and thicknesses of the crust are in agreement with Wieczorek and Zuber (2004). For the mantle, we consider five plausible Mars mantle compositions (Taylor, 2013; Sanloup et al., 1999; Lodders and Fegley, 1997; Mohapatra and Murty, 2003; Morgan and Anders, 1979) (denoted in the figures as: DW, EH45, LF, MM, and MA; these couples of letters usually refer to the names of the authors of the papers on mantle compositions, except for EH45) and two temperature end-members that have been deduced from 3D thermal-evolution studies (Plesa et al., 2016). The compositions have

Table 4: Mars rotation model to retrieve, along with the a priori constraints and post-fit uncertainties in the MOP estimates obtained with GINS using an iterative least square procedure. The nutation amplitudes are given for the rigid case (see Baland et al., 2019) and for the fluid core case (rigid/fluid), considering the nominal values for the Core momentum factor (liquid core amplification factor in Section 2 after Eq. (13)) and the FCN period. The LOD amplitudes are taken from Konopliv et al. (2016).

Parameter	Symbol	Nominal (Truth)	sol1 nom.	sol2 ext.	sol3 nut1	sol4 lod4	sol5 FCN	sol6 CW	sol7 RISE
Obliquity rate (mas/year)	$\dot{\varepsilon}_0$	-2.0	0.7	0.2	0.2	0.4	0.1	0.2	0.1
Precession rate (mas/year)	$\dot{\psi}_0$	-7608.3	1.5	0.4	0.5	0.9	0.3	0.6	0.3
1-annual cosine spin angle (mas)	ϕ_1^c	481	17	1	8	2	2	2	5
1/2-annual cosine spin angle (mas)	ϕ_2^c	-103	16	6	8	9	3	6	5
1/3-annual cosine spin angle (mas)	ϕ_3^c	-35				7			
1/4-annual cosine spin angle (mas)	ϕ_4^c	-10				1			
1-annual sine spin angle (mas)	ϕ_1^s	-155	18	2	7	4	3	3	6
1/2-annual sine spin angle (mas)	ϕ_2^s	-93	20	6	10	7	5	8	5
1/3-annual sine spin angle (mas)	ϕ_3^s	-3				11			
1/4-annual sine spin angle (mas)	ϕ_4^s	-8				1			
Core momentum factor (a priori)	F	0.07					0.02		
FCN period (days)	T_{FCN}	-240					4		
1-annual prograde nutation (mas)	p_1	102/104			5				4
1/2-annual prograde nutation (mas)	p_2	498/512	11	4	6	7		5	4
1/3-annual prograde nutation (mas)	p_3	108/112	5	3	3	4		4	2
1-annual retrograde nutation (mas)	r_1	137/132			6				4
1/2-annual retrograde nutation (mas)	r_2	18/15	15	4	8	5		5	3
1/3-annual retrograde nutation (mas)	r_3	5/12	10	4	4	8		6	2
Chandler wobble cosine (mas)	X_{cw}^c	33						4	
Chandler wobble sine (mas)	X_{cw}^s	33						4	
Chandler wobble cosine (mas)	Y_{cw}^c	33						6	
Chandler wobble sine (mas)	Y_{cw}^s	33						4	

been deduced from Martian meteorites and assumptions about Mars’ formation. Elastic properties of the mantle are calculated with **PerpleX** (Connolly, 2005) and those of the liquid Fe-S core are detailed in Rivoldini and Van Hoolst (2013). In order to calculate the interior structure, we integrate the Poisson equation (relating the gravitational potential to the density) and hydrostatic pressure equation (relating the pressure exerted at equilibrium to the gravity and density) in the whole planet and the adiabatic gradient equation in the core. Our models match Mars’ mass exactly, assume zero pressure at the surface, and continuity of pressure and gravity between crust, mantle, and core and continuity in temperature between the lower mantle and core. The system of ordinary differential equations and the associated boundary values are solved with **BVP Solver** (Boundary Value Problem) (Shampine et al., 2006). We have only retained models that agree at 1σ with the average moment of inertia ($\text{MoI} = 0.3638 \pm 0.0001$ (Konopliv et al., 2016)). Models with a solid inner core can also agree with the MoI but have denser and smaller cores and therefore do not agree with the tidal Love number k_2 (Rivoldini et al., 2011). For this reason, we do not consider models with a solid inner core in this study.

In a second step, the spherical models are deformed hydrostatically, i.e. it is assumed that they are fluid and rotating with the rotation period of Mars. The geometric flattening of the hydrostatic models are calculated by solving Clairaut’s equation (e.g. Moritz, 1990). The polar and equatorial moments of inertia of the planet and core can then be directly calculated starting from the geometric flattening.

The relation between core sulfur concentration and radius for the different mantle models and temperature profiles is shown in Fig. 16. The core radius range of the models results from the requirement that the models have a fully molten core (lower boundary) and are within 1σ of the MoI of Mars. Unlike models with the hotter mantle temperature, cold mantle models require more sulfur to remain completely molten and have a denser mantle and, therefore, a somewhat larger mantle moment of inertia at a given core radius. For this reason, the range of core radii that agrees with the MoI is reduced compared to hot mantle models.

The period of the FCN (Fig. 17a) increases with core radius because the dynamical flattening of the core mantle boundary increases faster than the moment inertia of the mantle (Eq. (11)). The FCN periods of the models are within the periods of the retrograde semi-annual and ter-annual (-343.5 days to -229 days) nutations and it can be expected that these nutations are the most affected by the liquid core (changes of 16% and 140% for r_2 and r_3 , respectively, for the truth model of Tab. 4).

The period of the CW (Fig. 17b) increases with core radius because the compliance κ increases faster than the moment of inertia of the mantle decreases (Eq. (8)). For all the considered models, the variation is less than 5 days, smaller than the expected precision of LaRa. This is the reason why this parameter is not estimated but fixed using its theoretical value.

The liquid core amplification factor F (Fig. 18a) increases with core radius or increasing moment of inertia of the core (Eq. (13)). It is only weakly dependent on the thermal state of the planet and mineralogy of the mantle and is therefore a robust estimator for the core radius. With the expected precision of LaRa and in the situation that the FCN resonance is weak, the core radius can be estimated with a precision of about 160 km assuming we will get a precision of 0.02 on F .

Among the considered nutations, the retrograde ter-annual rigid nutations is the most affected by the FCN normal mode (Fig. 19). In the hydrostatic equilibrium case, models with core radii about 2050 km could experience amplifications in excess of 100 mas because they have an FCN period that is very close to that of the retrograde ter-annual rigid nutation. Models with such large cores do, however, not agree with the observed tidal k_2 Love number at 1σ (Genova et al., 2016; Konopliv et al., 2016; Rivoldini et al., 2011; Khan et al., 2018). Geodesy constraints require that the core radius of Mars is between 1730 km and 1859 km (Rivoldini et al., 2011; Khan et al., 2018) (computed for hydrostatic equilibrium). For the whole set of core radii, a variation of the r_1 amplitude by 2 to 7 mas could be expected whereas r_3 can be amplified by up to few 100 mas and p_2 can vary between 5 and 20 mas (Fig. 19). With the expected precision provided by LaRa alone of 4 to 8 mas in r_3 and 4-7 mas in p_2 (see Tab. 4), the radius of the core could then be estimated with a precision of 1 to 300 km depending on the radius of the core. When using both RISE and LaRa (precision of 2 mas and 4 mas on r_3 and p_2), this estimation can be reduced and the precision ranges from 1 to 100 km depending on the radius of the core.

It is well known that the shape of Mars deviates significantly from the ellipsoidal shape of a purely hydrostatic planet of the same composition and size as Mars deformed from a fluid sphere by rotation. It is thought that this deviation is mainly the result of the large Martian volcanic provinces (e.g. Phillips et al., 2001). It can be expected that these mass anomalies also affect the hydrostatic shape of the core through their loading effect. Since the frequency of the FCN is almost linearly dependent on the dynamic flattening of the core (Eq. (11)), core radius estimations from the FCN period could be biased if the correct shape of the core were not taken into account. Conversely, if the radius of the core were already known - from the measured tides (Genova et al., 2016; Konopliv et al., 2016; Rivoldini et al., 2011), seismic sounding by the SEIS instrument on InSight (Panning et al., 2016), or from nutation amplitudes measured by RISE and LaRa - and if the effect on the period of the FCN is larger than the expected precision of the LaRa measurements, then the dynamic flattening of the core could be constrained. Unlike the FCN period, F does not depend directly on the dynamic flattening of the core and therefore core radius estimates based on F are more robust than those based on the FCN period. Partial melt layers in the mantle due to thermal effects or water could significantly affect the mantle rheology and the compliances, but they affect the FCN, F , and T_F only weakly since these parameters depend mainly on the moments of inertia of the planet and core. The effect of the rheology on nutations can be further reduced if prior knowledge about the mantle rheology deduced from the tidal dissipation factor of Mars is included in the modeling. Such a rheology reduces the FCN period by up to 1.5 days and F by up to 3%.

4.2.2 Constraints on the dynamic of Mars atmosphere

Today, the lack of continuous global observations of dynamical variables, i.e. with a good temporal and spatial resolution, limits studies of the dynamics of the Martian atmosphere. Although, currently, the overall agreement between the observed and modeled LOD variations is fairly good (Karatekin et al., 2017), the present knowledge of LOD is not sufficient enough to differ between models and to constrain Mars CO₂ cycle or winds. In addition, the accuracy of the observations is not sufficient to determine the polar motion or the interannual variability of the LOD. LaRa will improve the current precision on LOD more than an order of magnitude with respect to previous orbiter determinations. This improved precision will provide constraints on the details of the physical processes taking part in the angular momentum variations of the Martian atmosphere. In addition, with such a precision on LOD and with longer tracking coverage it might be possible to see

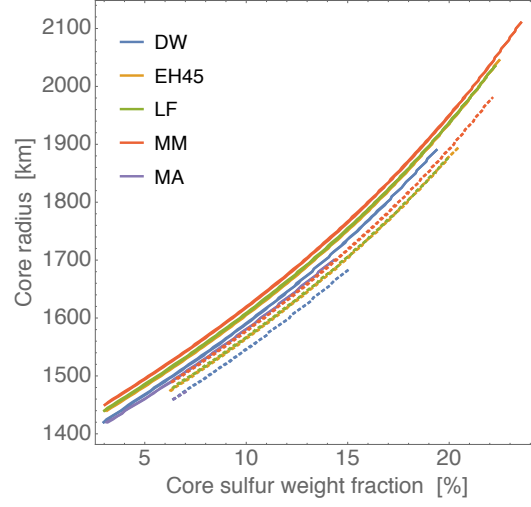


Figure 16: Core radius as a function of core sulfur concentration. Models using the cold temperature profile are shown by dotted lines.

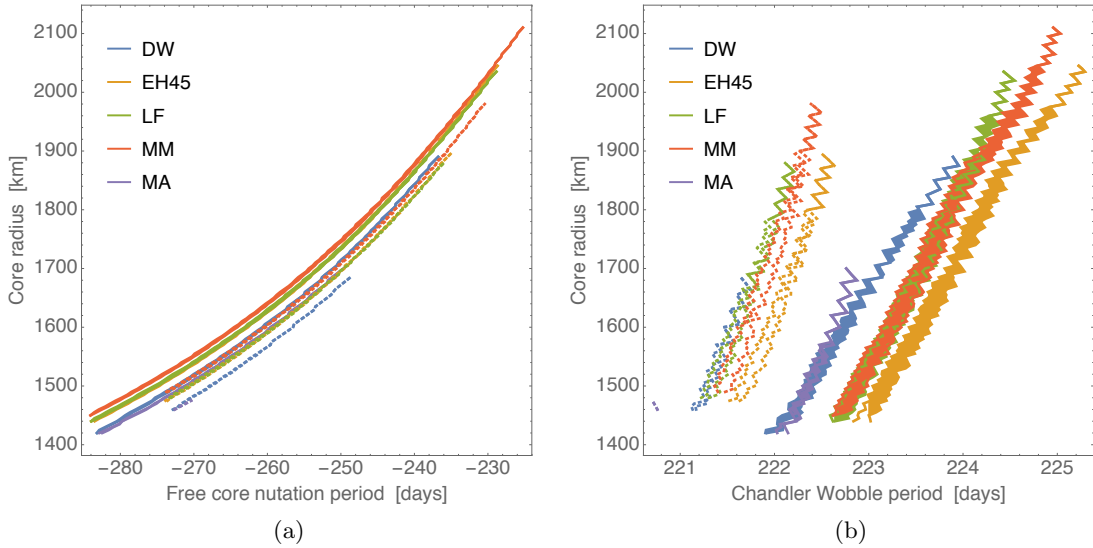


Figure 17: Core radius as a function of (a) Free Core Nutation period (in Inertial Frame) and (b) Chandler Wobble period (in co-rotating Body Frame). The models are built on an initial state in hydrostatic equilibrium. Models using the cold temperature profile are shown by dotted lines.

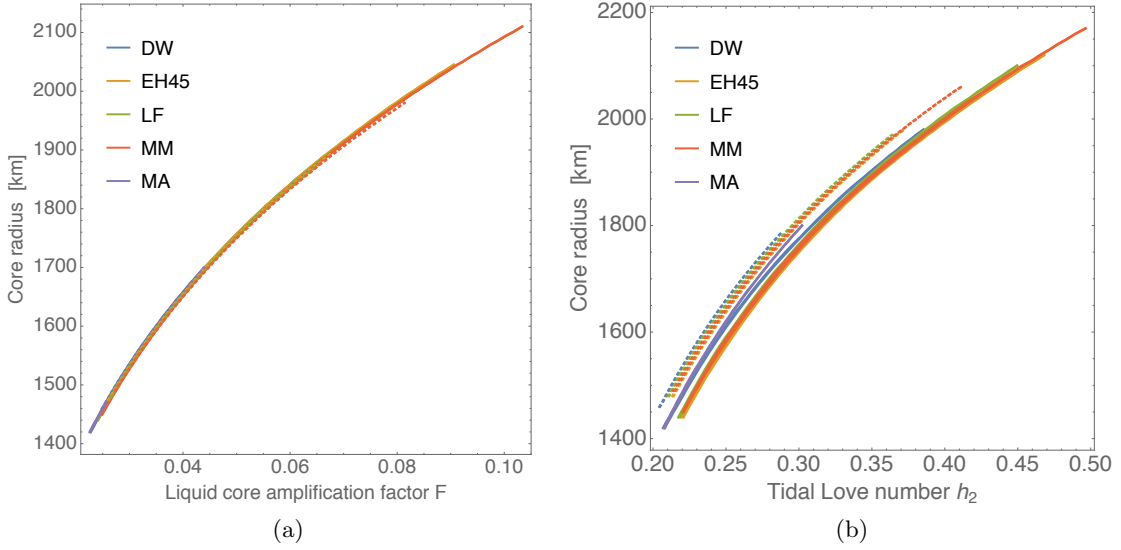


Figure 18: Core radius as a function of (a) liquid core amplification factor F (in Inertial Frame) and (b) tidal Love number h_2 (in co-rotating Body Frame). Models using the cold temperature profile are shown by dotted lines.

the inter-annual variations of the global-scale cycling of CO_2 on Mars that could arise from the dust storm variability. Furthermore determination of Chandler Wobble would provide information on the interior based on the value of the frequency as well as novel information on Mars' atmospheric dynamics in a band close to the CW frequency.

4.3 Surface platform positioning

Beside measuring the rotational motion of Mars, LaRa will accurately determine the location of the ExoMars Kazachok Platform at the surface of Mars early after landing. Indeed, after a few of hours of tracking, LaRa will allow determining the SP equatorial-plane coordinates (longitude, λ_0 and distance to spin axis, r_0) with high level of accuracy, while the Z_0 coordinate (along the spin axis) will only be estimated with 1-8 km depending on the actual number of tracking hours used to determine the lander location (see Fig. 20). The inefficiency of the Mars lander's DTE Doppler measurements to accurately determine the Z coordinate is well known (Le Maistre et al., 2012) and can be counterbalanced by forcing the lander's Z coordinate to tie the lander to the surface, as defined by a topography model. Using such a method proposed by Le Maistre (2016) and successfully applied by the ROB team for InSight, σ_{Z_0} will be reduced to about 10m (see Fig. 21), which is more than two orders of magnitude smaller than the uncertainty provided by DTE Doppler measurements alone.

An early estimate of the lander location will certainly improve the quality of the science analysis (for instance by making easier the recognition of the geological features seen on the lander's pictures) and allow high-resolution cameras from spacecraft to correctly target the lander. The advantage of Le Maistre (2016)'s approach is that it does not rely on measurements from orbiters, which might take extra time to acquire and deliver to Earth the lander imaging data that would allow to locate the spacecraft on the Martian terrain of the landing site.

After one Martian year of operation, LaRa will allow positioning the ExoMars 2020 Kaza-

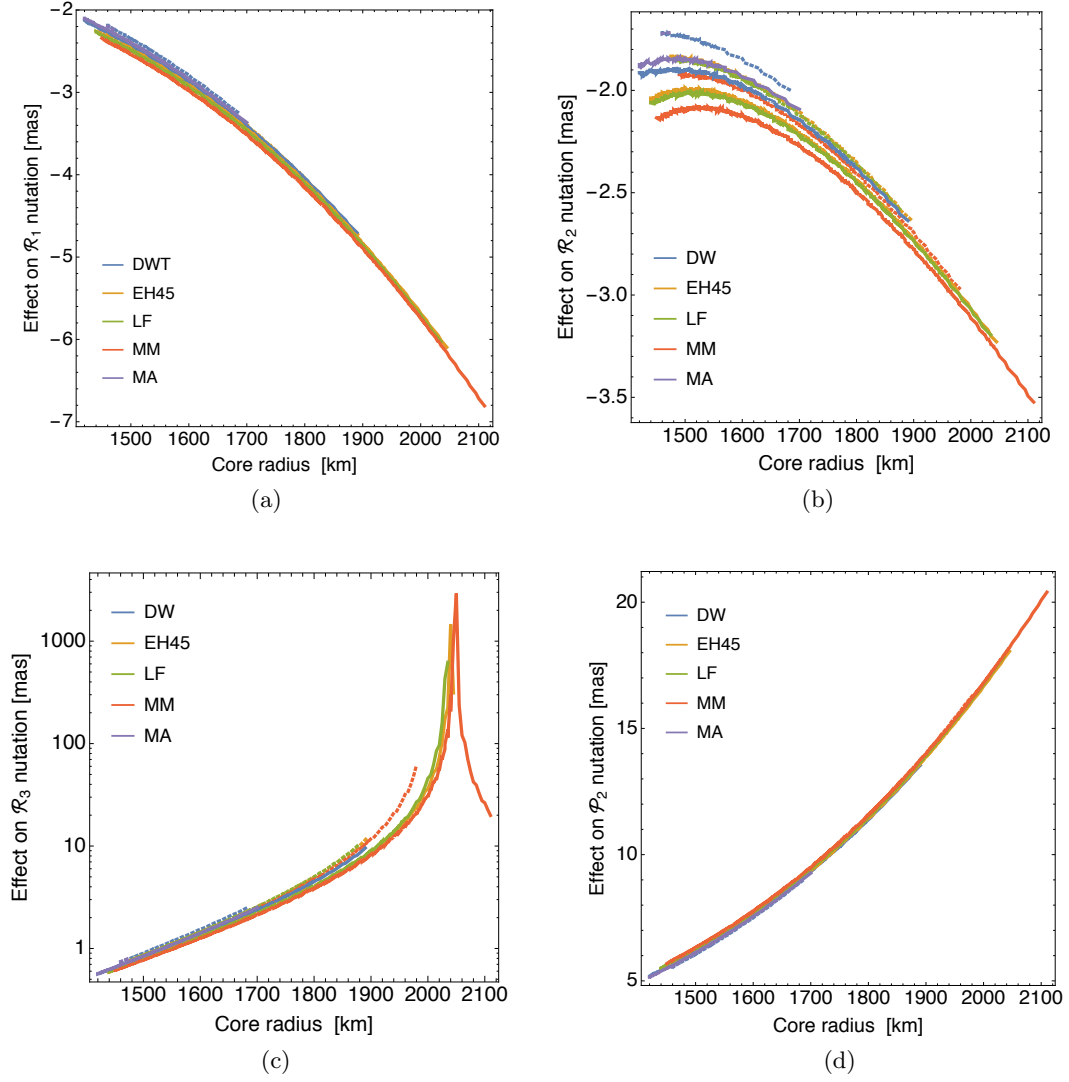


Figure 19: Effect of FCN rotational normal mode on (a) retrograde annual, (b) semi-annual, (c) ter-annual, and (d) prograde semi-annual nutations as a function of core radius. Models using the cold temperature profile are shown by dotted lines.

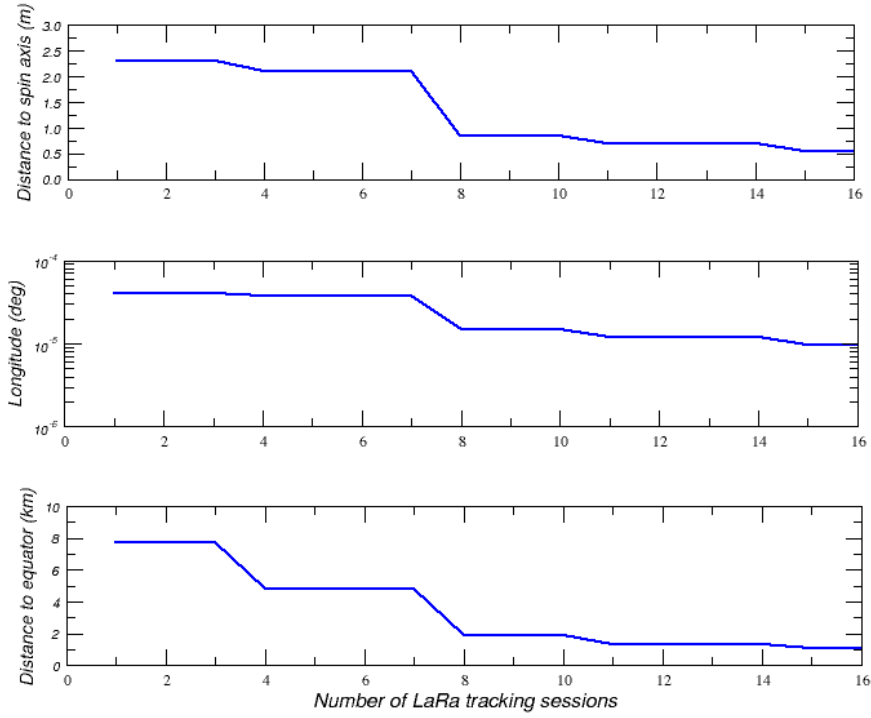


Figure 20: LaRa’s positioning of the ExoMars 2020 Surface Platform at the surface of Mars after few hours of tracking. The figure shows the time evolution of the uncertainties in r_0 (upper panel), in longitude, λ_0 (middle panel) and in Z_0 (lower panel).

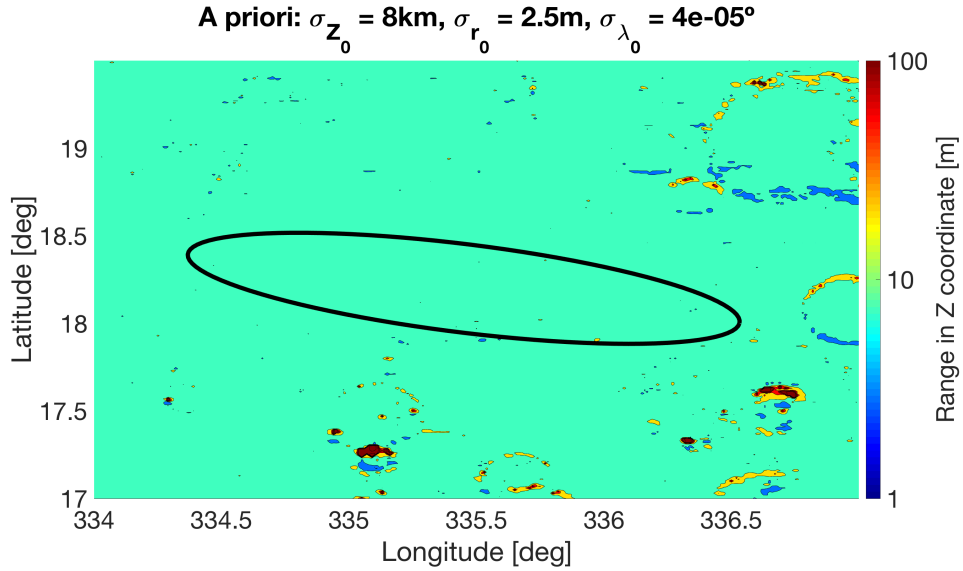


Figure 21: Range of allowed Z-coordinates as a function of the actual lander location inferred from a priori knowledge that we get after a couple of hours of DTE Doppler tracking of LaRa.

chok Surface Platform with an accuracy of less than 10cm for the equatorial-plane coordinates and few meters for the Z component.

5 Discussion and conclusions

Over the last decade, several missions involving either spacecraft orbiting Mars or landers or rovers on the surface have brought new understanding of the planet Mars, in particular on Mars’ evolution and habitability. However, the interior of Mars is still not yet well known. As the interior of a planet retains signatures of its origin and subsequent evolution, missions addressing that subject will allow us to answer some of the most debated questions of the moment.

The Earth’s interior is mainly constrained by seismic data from an extended network of seismometers. However, for Mars, there is no such network, though the seismic activity of Mars is currently monitored by the SEIS experiment on InSight (Lognonné et al., 2019). Till now, the existence of a liquid core inside Mars has been deduced from measuring tides (Yoder et al., 2003). In the future, independent determinations of the state of the core will be provided from measuring Mars’ rotation by the RISE experiment on InSight (Folkner et al., 2018) and by the LaRa experiment on ExoMars 2020. Besides determining the state of the core, precise measurements of Mars’ rotation and polar motion also allow to provide constraints about its shape and the energy in the atmosphere at seasonal timescale.

The paper has further addressed the understanding of the core, based on the determination of Mars’ rotation and orientation variations. The related scientific experiments on fixed landers on the surface observed from Earth with the help of radio signals are either just in place (RISE on InSight, landed on November 26, 2018) or will be in place (LaRa on ExoMars 2020, to land in 2021). The present paper has addressed the LaRa experiment in this perspective.

In Section 2, we have described the rotation of Mars, the models that are presently available and on which the LaRa experiment simulations have been based. In Section 3, we have described the LaRa instrument (a coherent transponder and three antennas working in X-band) and presented the possibilities that it allows in terms of science. In particular, the MOP (Mars Orientation and rotation Parameters) signatures have been studied and the interior parameters that can be reached have been presented in Section 4. We have discussed these parameters and have shown that the core amplification factor increases with core radius - or equivalently with the core moment of inertia (Eq. (13)) - and that it provides the best measurement of the core radius. Indeed, it is only weakly dependent on the thermal state of the planet and on the mantle mineralogy. With an expected precision of LaRa concerning the nutation amplitudes of 4 mas, the core radius can be estimated with a precision better than 160 km. The possibility of observing the FCN period from LaRa data depends on the actual value of the FCN, which depends on the core radius, the mantle rheology, the equilibrium state of the core (hydrostatic or not). The non-hydrostatic contribution was not discussed in this paper. It will shift the resonances to the CW and the FCN by about 20 days (a decrease from 220 to 200 days for the CW period and from -240 to -260 days for instance for the FCN period), but will not change the results of this paper. This paper represents an interesting information to envisage the future LaRa experiment in complement with the RISE experiment.

Further discussions and details on the impact of the operational and technical characteristics of LaRa on the nutation determination (Le Maistre et al., 2019) and on the complementarities between the RISE (Rotation and Interior Structure Experiment) experiment on InSight and the LaRa experiment (Péters et al., 2019) are provided in two companion papers.

6 Acknowledgments

For the Belgian authors, this work was financially supported by the Belgian PRODEX program managed by the European Space Agency in collaboration with the Belgian Federal Science Policy Office.

This project was made possible thanks to a dedicated team at the AntwerpSpace company, including Jean-François Boone, Lieven Thomassen, Donald Heyman, Felix Rautschke, Dave Bail, Bart Desoete, Wim Philibert, Vincent Bath, Koen Puimege, and their collaborators.

Finally, the LaRa science team would like to warmly thank Marline Claessens, Daniel Firre, Jean-Philippe Halain, Alberto Busso, Marco Sabbadini, Lorenzo Marchetti, Michel Lazerges and ESA personnel who supported the LaRa technical staff in the development of the instrument all over the project.

This research was carried out in part by the InSight Project at the Jet Propulsion Laboratory, California Institute of Technology, under contract with the National Aeronautics and Space Administration.

References

- B. A. Archinal, C. H. Acton, M. F. A’Hearn, A. Conrad, G. J. Consolmagno, T. Duxbury, D. Hestroffer, J. L. Hilton, R. L. Kirk, S. A. Klioner, D. McCarthy, K. Meech, J. Oberst, J. Ping, P. K. Seidelmann, D. J. Tholen, P. C. Thomas, and I. P. Williams. Report of the iau working group on cartographic coordinates and rotational elements: 2015. *Celestial Mechanics and Dynamical Astronomy*, 130(3):22, Feb 2018. ISSN 1572-9478. doi: 10.1007/s10569-017-9805-5. URL <https://doi.org/10.1007/s10569-017-9805-5>.
- S. W. Asmar, J. W. Armstrong, L. Iess, and P. Tortora. Spacecraft Doppler tracking: Noise budget and accuracy achievable in precision radio science observations. *Radio Science*, 40:RS2001, April 2005. doi: 10.1029/2004RS003101.
- R.-M. Baland, M. Yseboodt, S. Le Maistre, A. Rivoldini, T. Van Hoolst, and V. Dehant. The precession and nutations of a rigid Mars. *Celestial Mechanics and Dynamical Astronomy*, XX(In preparation):xx, 2019. doi: xxx.
- J.-P. Barriot, V. Dehant, W. Folkner, J.-C. Cerisier, A. Ribes, J. Benoist, T. van Hoolst, P. Defraigne, R. Warnant, R. A. Preston, L. Romans, S. Wu, and A. W. Wernik. The netlander ionosphere and geodesy experiment. *Advances in Space Research*, 28:1237–1249, 2001. doi: 10.1016/S0273-1177(01)00295-2.
- N. Bergeot, O. Witasse, S. Le Maistre, P.-L. Blelly, K. Wlodek, K. Peter, V. Dehant, and J.-M. Chevalier. MoMo: a new empirical model of the Mars ionospheric total electron content based on Mars Express MARSIS data. *J. Space Weather Sci.*, 2019. doi: 10.1051/swsc/2019035.
- T. M. Bocanegra-Bahamón, G. Molera Calvés, L. I. Gurvits, D. A. Duev, S. V. Pogrebenko, G. Cimò, D. Dirkx, and P. Rosenblatt. Planetary Radio Interferometry and Doppler Experiment (PRIDE) technique: A test case of the Mars Express Phobos Flyby. II. Doppler tracking: Formulation of observed and computed values, and noise budget. *Astr. Astrophys.*, 609:A59, January 2018. doi: 10.1051/0004-6361/201731524.
- T. M. Bocanegra-Bahamón, G. Molera Calvés, L. I. Gurvits, G. Cimò, D. Dirkx, D. A. Duev, S. V. Pogrebenko, P. Rosenblatt, S. Limaye, L. Cui, P. Li, T. Kondo, M. Sekido, A. G. Mikhailov, M. A. Kharinov, A. V. Ipatov, W. Wang, W. Zheng, M. Ma, J. E. J.

- Lovell, and J. N. McCallum. Venus Express radio occultation observed by PRIDE. *Astr. Astrophys.*, 624:A59, Apr 2019. doi: 10.1051/0004-6361/201833160.
- N. Borderies, G. Balmino, L. Castel, and B. Moynot. Study of Mars dynamics from lander tracking data analysis. *Moon and Planets*, 22:191–200, April 1980. doi: 10.1007/BF00898430.
- S. Bouquillon and J. Souchay. Precise modeling of the precession-nutation of Mars. *Astronomy and Astrophysics*, 345(1):282–297, 1999.
- Wei Chen and WenBin Shen. New estimates of the inertia tensor and rotation of the triaxial nonrigid earth. *J. Geophys. Res.*, 115(B12):B12419, 12 2010.
- J. A. D. Connolly. Computation of phase equilibria by linear programming: A tool for geodynamic modeling and its application to subduction zone decarbonation. *Earth and Planetary Science Letters*, 236(1–2):524–541, 7 2005.
- P. Defraigne, V. Dehant, and P. Pâquet. Link between the Retrograde-Prograde Nutations and Nutations in Obliquity and Longitude. *Celestial Mechanics and Dynamical Astronomy*, 62:363–376, December 1995. doi: 10.1007/BF00692286.
- P. Defraigne, O. de Viron, V. Dehant, T. Van Hoolst, and F. Hourdin. Mars rotation variations induced by atmosphere and ice caps. *Journal of Geophysical Research Planets*, 105:24563–24570, October 2000. doi: 10.1029/1999JE001227.
- P. Defraigne, A. Rivoldini, T. Van Hoolst, and V. Dehant. Mars nutation resonance due to Free Inner Core Nutation. *J. Geophys. Res. (Planets)*, 108:2–1, December 2003.
- V. Dehant and P. M. Mathews. *Precession, Nutation and Wobble of the Earth*. Cambridge University Press, 2015.
- V. Dehant, P. Lognonné, and C. Sotin. Network science, NetLander: a european mission to study the planet Mars. *Planetary and Space Science*, 52:977–985, September 2004. doi: 10.1016/j.pss.2004.07.019.
- V. Dehant, T. van Hoolst, S. Le Maistre, O. Karatekin, M. Beuthe, P. Rosenblatt, M. Yseboodt, J. Duron, and J. P. Barriot. Radio science opportunities on Mars with an orbiter and lander(s). In *European Planetary Science Congress 2006*, volume 1, page 188, 2006.
- V. Dehant, W. Folkner, E. Renotte, D. Orban, S. Asmar, G. Balmino, J.-P. Barriot, J. Benoist, R. Biancale, J. Biele, F. Budnik, S. Burger, O. de Viron, B. Häusler, Ö. Karatekin, S. Le Maistre, P. Lognonné, M. Menvielle, M. Mitrovic, M. Pätzold, A. Rivoldini, P. Rosenblatt, G. Schubert, T. Spohn, P. Tortora, T. van Hoolst, O. Witasse, and M. Yseboodt. Lander radioscience for obtaining the rotation and orientation of Mars. *Planetary and Space Science*, 57:1050–1067, July 2009a. doi: 10.1016/j.pss.2008.08.009.
- V. Dehant, S. Le Maistre, P. Rosenblatt, M. Mitrovic, D. Orban, A. Rivoldini, J. Marty, and T. van Hoolst. Rotation and interior of Mars from radioscience. *AGU Fall Meeting Abstracts*, December 2009b.
- V. Dehant, S. Le Maistre, A. Rivoldini, M. Yseboodt, P. Rosenblatt, T. Van Hoolst, M. Mitrovic, Ö. Karatekin, J.C. Marty, and A. Chicarro. Revealing mars’ deep interior: Future geodesy missions using radio links between landers, orbiters, and the earth. *Planetary and Space Science*, 59:1069–1081, 2011. ISSN 0032-0633. doi: 10.1016/j.pss.2010.03.014.

- Veronique Dehant, Bruce Banerdt, Philippe Lognonne, Matthias Grott, Sami Asmar, Jens Biele, Doris Breuer, Francois Forget, Ralf Jaumann, Catherine Johnson, Martin Knapmeyer, Benoit Langlais, Mathieu Le Feuvre, David Mimoun, Antoine Mocquet, Peter Read, Attilio Rivoldini, Oliver Romberg, Gerald Schubert, Sue Smrekar, Tilman Spohn, Paolo Tortora, Stephan Ulamec, and Susanne Vennerstrom. Future mars geophysical observatories for understanding its internal structure, rotation, and evolution. *Planetary and Space Science*, 68(1):123–145, 2012. ISSN 0032-0633. doi: 10.1016/j.pss.2011.10.016. URL <http://www.sciencedirect.com/science/article/pii/S0032063311003278>. Terrestrial Planets 1.
- D. A. Duev, G. Molera Calvés, S. V. Pogrebenko, L. I. Gurvits, G. Cimó, and T. Bocanegra Bahamon. Spacecraft VLBI and Doppler tracking: algorithms and implementation. *Astronomy and Astrophysics*, 541:A43, May 2012. doi: 10.1051/0004-6361/201218885.
- D. A. Duev, S. V. Pogrebenko, G. Cimò, G. Molera Calvés, T. M. Bocanegra Bahamón, L. I. Gurvits, M. M. Kettenis, J. Kania, V. Tudose, P. Rosenblatt, J.-C. Marty, V. Lainey, P. de Vicente, J. Quick, M. Nickola, A. Neidhardt, G. Kronschnabl, C. Ploetz, R. Haas, M. Lindqvist, A. Orlati, A. V. Ipatov, M. A. Kharinov, A. G. Mikhailov, J. E. J. Lovell, J. N. McCallum, J. Stevens, S. A. Gulyaev, T. Natush, S. Weston, W. H. Wang, B. Xia, W. J. Yang, L.-F. Hao, J. Kallunki, and O. Witasse. Planetary Radio Interferometry and Doppler Experiment (PRIDE) technique: A test case of the Mars Express Phobos fly-by. *Astronomy and Astrophysics*, 593:A34, September 2016. doi: 10.1051/0004-6361/201628869.
- Y. Fei, J. Li, C. M. Bertka, and C. T. Prewitt. Structure type and bulk modulus of Fe_3S , a new iron-sulfur compound. *American Mineralogist*, 85(11-12):1830–1833, November 2000.
- J. Feltens, G. Bellei, T. Springer, M.V. Kints, R. Zandbergen, F. Budnik, and E. Schönmann. Tropospheric and ionospheric media calibrations based on global navigation satellite system observation data. *J. Space Weather Space Clim.*, 8(A30):23, 2018. doi: 10.1051/swsc/2018016.
- W. M. Folkner, R. D. Kahn, R. A. Preston, C. F. Yoder, E. M. Standish, J. G. Williams, C. D. Edwards, R. W. Hellings, T. M. Eubanks, and B. G. Bills. Mars dynamics from Earth-based tracking of the Mars Pathfinder lander. *Journal of Geophysical Research Planets*, 102:4057–4064, February 1997a. doi: 10.1029/96JE02125.
- W. M. Folkner, C. F. Yoder, D. N. Yuan, E. M. Standish, and R. A. Preston. Interior Structure and Seasonal Mass Redistribution of Mars from Radio Tracking of Mars Pathfinder. *Science*, 278:1749–1751, December 1997b. doi: 10.1126/science.278.5344.1749.
- W. M. Folkner, V. Dehant, S. Le Maistre, M. Yseboodt, A. Rivoldini, T. Van Hoolst, S. Asmar, and M. Golombek. The Rotation and Interior Structure Experiment on the InSight Mission to Mars. *Space Science Reviews*, 214(5):100, August 2018.
- A. Genova, S. Goossens, F. G. Lemoine, E. Mazarico, G. A. Neumann, D. E. Smith, and M. T. Zuber. Seasonal and static gravity field of Mars from MGS, Mars Odyssey and MRO radio science. *Icarus*, 272:228–245, July 2016. doi: 10.1016/j.icarus.2016.02.050.
- H. Harder and U. R. Christensen. A one-plume model of martian mantle convection. *Nature*, 380:507–509, April 1996. doi: 10.1038/380507a0.
- A.-M. Harri, O. Marsal, P. Lognonne, G. W. Leppelmeier, T. Spohn, K.-H. Glassmeier, F. Angrilli, W. B. Banerdt, J. P. Barriot, J.-L. Bertaux, J. J. Berthelier, S. Calcutt, J. C.

- Cerisier, D. Crisp, V. Dehant, D. Giardini, R. Jaumann, Y. Langevin, M. Menvielle, G. Musmann, J. P. Pommereau, S. di Pippo, D. Guerrier, K. Kumpulainen, S. Larsen, A. Mocquet, J. Polkko, J. Runavot, W. Schumacher, T. Siili, J. Simola, and J. E. Tillman. Network science landers for Mars. *Advances in Space Research*, 23:1915–1924, January 1999. doi: 10.1016/S0273-1177(99)00279-3.
- M. A. Kahre, J. L. Hollingsworth, R. M. Haberle, and R. J. Wilson. Coupling the Mars dust and water cycles: The importance of radiative-dynamic feedbacks during northern hemisphere summer. *Icarus*, 260:477–480, Nov 2015. doi: 10.1016/j.icarus.2014.07.017.
- Melinda A. Kahre and Robert M. Haberle. Mars CO₂ cycle: Effects of airborne dust and polar cap ice emissivity. *Icarus*, 207(2):648–653, Jun 2010. doi: 10.1016/j.icarus.2009.12.016.
- ö. Karatekin and L. Montabone. Atmospheric Angular Momentum and Rotation Variations of Mars between Martian years 24 and 27. In F. Forget and M. Millour, editors, *Mars Atmosphere: Modelling and Observation, 5th International Workshop*, page 1311, January 2014.
- Ö. Karatekin, J. Duron, P. Rosenblatt, T. Van Hoolst, V. Dehant, and J.-P. Barriot. Mars’ time-variable gravity and its determination: Simulated geodesy experiments. *Journal of Geophysical Research (Planets)*, 110:E06001, June 2005. doi: 10.1029/2004JE002378.
- Ö. Karatekin, O. de Viron, S. Lambert, V. Dehant, P. Rosenblatt, T. van Hoolst, and S. Le Maistre. Atmospheric angular momentum variations of Earth, Mars and Venus at seasonal time scales. *Planetary and Space Science*, 59:923–933, August 2011. doi: 10.1016/j.pss.2010.09.010.
- O. Karatekin, V. Dehant, S. Le Maistre, S. Asmar, and A. Konopliv. Radioscience Experiments to Monitor Atmospheric Angular Momentum Variations Onboard the Forthcoming 2018 Insight and 2020 ExoMars Landers. In F. Forget and M. Millour, editors, *The Mars Atmosphere: Modelling and observation*, page 4417, January 2017.
- S. Karki, M. Sabbadini, K. Alkhalifeh, and C. Craeye. Metallic Monopole Parasitic Antenna with Circularly Polarized Conical Patterns. *IEEE Transactions on Antennas and Propagation*, 67(8):5243–5252, April 2019.
- A. Khan, C. Liebske, A. Rozel, A. Rivoldini, F. Nimmo, J. A. D. Connolly, A. C. Plesa, and D. Giardini. A Geophysical Perspective on the Bulk Composition of Mars. *Journal of Geophysical Research: Planets*, 123:575–611, 2018.
- J. A. Klobuchar. Ionospheric time-delay algorithm for single-frequency GPS users. *IEEE Transactions on Aerospace Electronic Systems*, 23:325–331, May 1987. doi: 10.1109/TAES.1987.310829.
- A. S. Konopliv, C. F. Yoder, E. M. Standish, D.-N. Yuan, and W. L. Sjogren. A global solution for the Mars static and seasonal gravity, Mars orientation, Phobos and Deimos masses, and Mars ephemeris. *Icarus*, 182:23–50, May 2006. doi: 10.1016/j.icarus.2005.12.025.
- A. S. Konopliv, S. W. Asmar, B. G. Bills, N. Mastrodemos, R. S. Park, C. A. Raymond, D. E. Smith, and M. T. Zuber. The Dawn Gravity Investigation at Vesta and Ceres. *Space Science Reviews*, 163:461–486, December 2011a. doi: 10.1007/s11214-011-9794-8.
- A. S. Konopliv, S. W. Asmar, W. M. Folkner, Ö. Karatekin, D. C. Nunes, S. E. Smrekar, C. F. Yoder, and M. T. Zuber. Mars high resolution gravity fields from MRO, Mars

- seasonal gravity, and other dynamical parameters. *Icarus*, 211:401–428, January 2011b. doi: 10.1016/j.icarus.2010.10.004.
- A. S. Konopliv, R. S. Park, and W. M. Folkner. An improved JPL Mars gravity field and orientation from Mars orbiter and lander tracking data. *Icarus*, 274:253–260, August 2016. doi: 10.1016/j.icarus.2016.02.052.
- P. Kuchynka, W. M. Folkner, A. S. Konopliv, R. S. Park, S. Le Maistre, and V. Dehant. New constraints on Mars rotation determined from radiometric tracking of the Opportunity Mars Exploration Rover. *Icarus*, 229:340–347, February 2014. ISSN 0019-1035. doi: 10.1016/j.icarus.2013.11.015.
- Y. Langevin, J. P. Bibring, F. Montmessin, F. Forget, M. Vincendon, S. Douté, F. Poulet, and B. Gondet. Observations of the south seasonal cap of Mars during recession in 2004-2006 by the OMEGA visible/near-infrared imaging spectrometer on board Mars Express. *Journal of Geophysical Research (Planets)*, 112(E8):E08S12, Jul 2007. doi: 10.1029/2006JE002841.
- Yves Langevin, Sylvain Douté, Mathieu Vincendon, François Poulet, Jean-Pierre Bibring, Brigitte Gondet, Bernard Schmitt, and F. Forget. No signature of clear CO₂ ice from the ‘cryptic’ regions in Mars’ south seasonal polar cap. *nature*, 442(7104):790–792, Aug 2006. doi: 10.1038/nature05012.
- S. Le Maistre. *The rotation of Mars and Phobos from Earth-based radio-tracking observations of a lander*. PhD thesis, Université Catholique de Louvain, November 2013.
- S. Le Maistre. InSight coordinates determination from direct-to-Earth radio-tracking and Mars topography model. *Planetary and Space Science*, 121:1–9, February 2016. doi: 10.1016/j.pss.2015.11.003.
- S. Le Maistre, P. Rosenblatt, A. Rivoldini, V. Dehant, J-C. Marty, and Ö. Karatekin. Lander radio science experiment with a direct link between Mars and the Earth. *Planetary and Space Science*, 68(1):105–122, July 2012. ISSN 0032-0633. doi: 10.1016/j.pss.2011.12.020.
- S. Le Maistre, V. Dehant, and J-C. Marty. Mars nutation estimates from radio-tracking of landed missions prior to InSight and ExoMars 2020. In *European Planetary Science Congress*, September 2018a.
- S. Le Maistre, P. Rosenblatt, V. Dehant, J-C. Marty, and M. Yseboodt. Mars rotation determination from a moving rover using doppler tracking data: What could be done? *Planetary and Space Science*, 159:17–27, 2018b. doi: 10.1016/j.pss.2018.03.020. URL <http://www.sciencedirect.com/science/article/pii/S003206331730288X>.
- S. Le Maistre, M.-J. Péters, J-C. Marty, and V. Dehant. On the impact of the operational and technical characteristics of the LaRa experiment on the nutation determination. *Planet. Space Sci.*, *submitted*, 2019.
- K. Lodders and B. Fegley. An Oxygen Isotope Model for the Composition of Mars. *Icarus*, 126:373–394, April 1997.
- P. Lognonné, D. Giardini, B. Banerdt, J. Gagnepain-Beyneix, A. Mocquet, T. Spohn, J. F. Karczewski, P. Schibler, S. Cacho, W. T. Pike, C. Cavoit, A. Desautez, M. Favède, T. Gabsi, L. Simoulin, N. Striebig, M. Campillo, A. Deschamp, J. Hinderer, J. J. Lévêque, J. P. Montagner, L. Rivéra, W. Benz, D. Breuer, P. Defraigne, V. Dehant, A. Fujimura, H. Mizutani, and J. Oberst. The NetLander very broad

- band seismometer. *Planetary and Space Science*, 48:1289–1302, October 2000. doi: 10.1016/S0032-0633(00)00110-0.
- P. Lognonné, W.B. Banerdt, D. Giardini, W.T. Pike, U. Christensen, and the SEIS team. SEIS: The Seismic Experiment for Internal Structure of InSight. *Space Science Reviews, InSight pre-launch special issue*, 215:Id. 12, 2019. doi: 10.1007/s11214-018-0574-6.
- William Lowrie. *A Student's Guide to Geophysical Equations*. Cambridge University Press, Cambridge, 2011.
- P. M. Mathews, B. A. Buffett, T. A. Herring, and I. I. Shapiro. Forced nutations of the earth: Influence of inner core dynamics. I - Theory. *Journal of Geophysical Research*, 96:8219–8257, May 1991.
- R. K. Mohapatra and S. V. S. Murty. Precursors of Mars: Constraints from nitrogen and oxygen isotopic compositions of martian meteorites. *Meteoritics and Planetary Science*, 38:225–242, February 2003.
- G. Molera Calvés, E. Kallio, G. Cimò, J. Quick, D. A. Duev, T. Bocanegra Bahamón, M. Nickola, M. A. Kharinov, and A. G. Mikhailov. Analysis of an Interplanetary Coronal Mass Ejection by a Spacecraft Radio Signal: A Case Study. *Space Weather*, 15(11): 1523–1534, Nov 2017. doi: 10.1002/2017SW001701.
- D. D. Morabito and S. W. Asmar. Radio-Science Performance Analysis Software. *Telecommunications and Data Acquisition Progress Report*, 120:121–152, October 1994.
- J. W. Morgan and E. Anders. Chemical composition of Mars. *Geochimica et Cosmochimica Acta*, 43:1601–1610, October 1979.
- Helmut Moritz. *The Figure of the Earth. Theoretical Geodesy and the Earth's Interior*. Herbert Wichman, 1990.
- Mark P. Panning, Philippe Lognonné, W. Bruce Banerdt, Raphaël Garcia, Matthew Golombek, Sharon Kedar, Brigitte Knapmeyer-Endrun, Antoine Mocquet, Nick A. Teanby, Jeroen Tromp, Renee Weber, Eric Beucler, Jean-Francois Blanchette-Guertin, Ebru Bozdağ, Mélanie Drilleau, Tamara Gudkova, Stefanie Hempel, Amir Khan, Vedran Lekić, Naomi Murdoch, Ana-Catalina Plesa, Atillio Rivoldini, Nicholas Schmerr, Youyi Ruan, Olivier Verhoeven, Chao Gao, Ulrich Christensen, John Clinton, Veronique Dehant, Domenico Giardini, David Mimoun, W. Thomas Pike, Sue Smrekar, Mark Wieczorek, Martin Knapmeyer, and James Wookey. Planned Products of the Mars Structure Service for the InSight Mission to Mars. *Space Science Reviews*, pages 1–40, November 2016.
- M. Pätzold, T. Andert, M. Hahn, S. W. Asmar, J. P. Barriot, M. K. Bird, B. Häusler, K. Peter, S. Tellmann, E. Grün, P. R. Weissman, H. Sierks, L. Jorda, R. Gaskell, F. Preusker, and F. Scholten. A homogeneous nucleus for comet 67p/churyumov–gerasimenko from its gravity field. *Nature*, 530(7588):63–65, 02 2016. URL <http://dx.doi.org/10.1038/nature16535>.
- M.-J. Péters, S. Le Maistre, M. Yseboodt, A. Rivoldini, J.-C. Marty, and V. Dehant. Improving determination of the Martian rotation parameters through the synergy between LaRa and RISE radioscience experiments. *Planet. Space Sci.*, *accepted*, 2019.
- Roger J. Phillips, Maria T. Zuber, Sean C. Solomon, Matthew P. Golombek, Bruce M. Jakosky, W. Bruce Banerdt, David E. Smith, Rebecca M. E. Williams, Brian M. Hynek, Oded Aharonson, and Steven A. Hauck II. Ancient Geodynamics and Global-Scale Hydrology on Mars. *Science*, 291(5513):2587, 03 2001.

- Sylvain Piqueux, Armin Kleinböhl, Paul O. Hayne, David M. Kass, John T. Schofield, and Daniel J. McCleese. Variability of the martian seasonal CO₂ cap extent over eight Mars Years. *Icarus*, 251:164–180, May 2015. doi: 10.1016/j.icarus.2014.10.045.
- A. C. Plesa, M. Grott, N. Tosi, D. Breuer, T. Spohn, and M. A. Wieczorek. How large are present-day heat flux variations across the surface of Mars? *Journal of Geophysical Research: Planets*, 121(12):2386–2403, 2016.
- R. D. Reasenberg and R. W. King. The rotation of Mars. *Journal of Geophysical Research*, 84:6231–6240, October 1979. doi: 10.1029/JB084iB11p06231.
- A. Rivoldini and T. Van Hoolst. The interior structure of Mercury constrained by the low-degree gravity field and the rotation of Mercury. *Earth and Planetary Science Letters*, 377–378(0):62–72, 9 2013.
- A. Rivoldini, T. van Hoolst, L. Koot, S. Le Maistre, and V. Dehant. Probing the interior structure of Mars by studying its rotation. In *EPSC-DPS Joint Meeting 2011*, volume 6, page 1445, October 2011.
- A. Rivoldini, T. Van Hoolst, O. Verhoeven, A. Mocquet, and V. Dehant. Geodesy constraints on the interior structure and composition of Mars. *Icarus*, 213(2):451–472, June 2011.
- F. Roosbeek. Analytical Developments of Rigid Mars Nutation and Tide Generating Potential Series. *Celestial Mechanics and Dynamical Astronomy*, 75:287–300, 1999.
- C. Sanloup, A. Jambon, and P. Gillet. A simple chondritic model of Mars. *Phys. Earth Planet. Inter.*, 112:43–54, March 1999.
- F. Seitz and M. Schmidt. Atmospheric and oceanic contributions to Chandler wobble excitation determined by wavelet filtering. *Journal of Geophysical Research (Solid Earth)*, 110(B11):B11406, Nov 2005. doi: 10.1029/2005JB003826.
- L. F. Shampine, P. H. Muir, and H. Xu. A user-friendly Fortran BVP solver. *Journal of Numerical Analysis, Industrial and Applied Mathematics*, 1(2), 2006.
- K. Shin. Frequency and channel assignments. *JPL DSN Deep Space Network Series*, 810-005, 201, Rev. C, 2014.
- S. E. Smrekar, P. Lognonné, T. Spohn, W. B. Banerdt, D. Breuer, U. Christensen, V. Dehant, M. Drilleau, W. Folkner, N. Fuji, R. F. Garcia, D. Giardini, M. Golombek, M. Grott, T. Gudkova, C. Johnson, A. Khan, B. Langlais, A. Mittelholz, A. Mocquet, R. Myhill, M. Panning, C. Perrin, T. Pike, A.-C. Plesa, A. Rivoldini, H. Samuel, S. C. Stähler, M. van Driel, T. Van Hoolst, O. Verhoeven, R. Weber, and M. Wieczorek. Pre-mission InSights on the Interior of Mars. *Space Science Reviews*, 215:3, January 2019. doi: 10.1007/s11214-018-0563-9.
- G. Jeffrey Taylor. The bulk composition of Mars. *Chemie der Erde - Geochemistry*, 73(4):401–420, 12 2013.
- E. Van den Acker, T. Van Hoolst, O. de Viron, P. Defraigne, F. Forget, F. Hourdin, and V. Dehant. Influence of the seasonal winds and the CO₂ mass exchange between atmosphere and polar caps on Mars’ rotation. *Journal of Geophysical Research (Planets)*, 107:5055, July 2002. doi: 10.1029/2000JE001539.

- T. Van Hoolst and V. Dehant. Influence of triaxiality and second-order terms in flattenings on the rotation of terrestrial planets: I. Formalism and rotational normal modes. *Physics of the Earth and Planetary Interiors*, 134(1):17–33, 2002.
- T. Van Hoolst, V. Dehant, and P. Defraigne. Sensitivity of the Free Core Nutation and the Chandler Wobble to changes in the interior structure of Mars. *Physics of the Earth and Planetary Interiors*, 117:397–405, January 2000a.
- T. Van Hoolst, V. Dehant, and P. Defraigne. Chandler wobble and Free Core Nutation for Mars. *Planetary and Space Science*, 48:1145–1151, October 2000b.
- T. Van Hoolst, V. Dehant, F. Roosbeek, and P. Lognonné. Tidally induced surface displacements, external potential variations, and gravity variations on Mars. *Icarus*, 161(2):281–296, 2 2003. doi: 10.1016/S0019-1035(02)00045-3.
- P. van Thienen, N. J. Vlaar, and A. P. van den Berg. Assessment of the cooling capacity of plate tectonics and flood volcanism in the evolution of Earth, Mars and Venus. *Physics of the Earth and Planetary Interiors*, 150:287–315, June 2005. doi: 10.1016/j.pepi.2004.11.010.
- P. van Thienen, A. Rivoldini, T. Van Hoolst, and P. Lognonné. A top-down origin for martian mantle plumes. *Icarus*, 185:197–210, November 2006. doi: 10.1016/j.icarus.2006.06.008.
- M. A. Wieczorek and M. T. Zuber. Thickness of the Martian crust: Improved constraints from geoid-to-topography ratios. *J. Geophys. Res. (Planets)*, 109(E18):E01009, January 2004.
- O. Witasse, N. Altobelli, S. Barabash, L. Bruzzone, M. Dougherty, C. Erd, L. Fletcher, R. Gladstone, O. Grasset, L. Gurvits, P. Hartogh, H. Hussmann, I. Iess, Y. Langevin, P. Palumbo, G. Piccioni, G. Sarri, D. Titov, and J. E. Wahlund. JUICE: A European Mission to Jupiter and its Icy Moons. In *European Planetary Science Congress*, pages EPSC2015–564, Oct 2015.
- C. F. Yoder and E. M. Standish. Martian precession and rotation from Viking lander range data. *Journal of Geophysical Research Planets*, 102:4065–4080, 1997. doi: 10.1029/96JE03642.
- C. F. Yoder, A. S. Konopliv, D. N. Yuan, E. M. Standish, and W. M. Folkner. Fluid Core Size of Mars from Detection of the Solar Tide. *Science*, 300:299–303, April 2003. doi: 10.1126/science.1079645.
- M. Yseboodt, V. Dehant, and Marie-Julie Péters. Signatures of the martian rotation parameters in the doppler and range observables. *Planetary and Space Science*, 144: 74–88, 2017a. ISSN 0032-0633. doi: 10.1016/j.pss.2017.05.008.
- M. Yseboodt, A. Rivoldini, S. Le Maistre, and V. M. A. Dehant. Estimation of the interior parameters from Mars nutations and from Doppler measurements. *AGU Fall Meeting Abstracts*, December 2017b.
- Marie Yseboodt, Jean-Pierre Barriot, and Véronique Dehant. Analytical modeling of the Doppler tracking between a lander and a Mars orbiter in terms of rotational dynamics. *Journal of Geophysical Research (Planets)*, 108(E7):5076, Jul 2003. doi: 10.1029/2003JE002045.

M. T. Zuber, F. G. Lemoine, D. E. Smith, A. S. Konopliv, S. E. Smrekar, and S. W. Asmar. Mars Reconnaissance Orbiter Radio Science Gravity Investigation. *Journal of Geophysical Research (Planets)*, 112:E05S07, May 2007. doi: 10.1029/2006JE002833.